CHALMERS
UNIVERSITY OF TECHNOLOGY

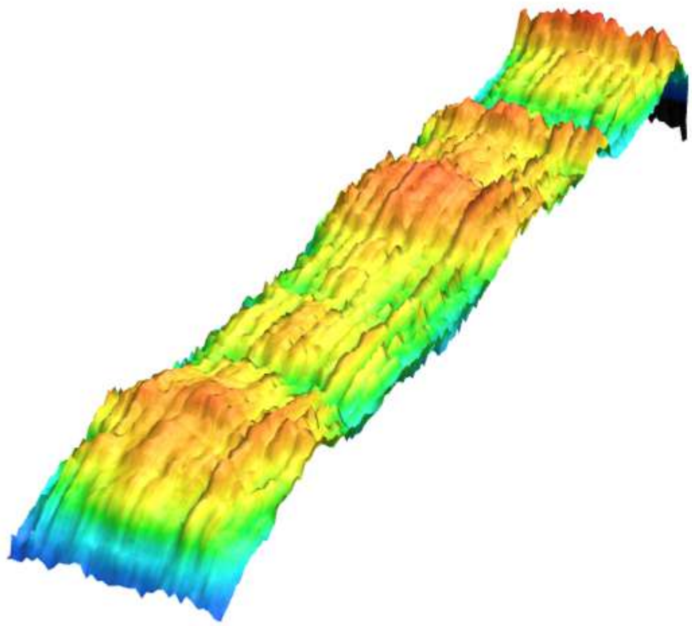

How Micro-Geometry of Cutting Edges Influences Surface Integrity

An Experimental Study on the Effects of Cutting Edge Micro-Geometry and Its Influence on the Surface Integrity of Machined Surfaces

Master's thesis in Production Engineering

ISAK NILSSON
KARL STEEN

DEPARTMENT OF MECHANICAL ENGINEERING

Chalmers University of Technology
Gothenburg, Sweden 2026
www.chalmers.se

Master's thesis 2026

How Micro-Geometry of Cutting Edges Influences Surface Integrity

An Experimental Study on the Effects of Cutting Edge Micro-Geometry and Its Influence on the Surface Integrity of Machined Surfaces

Isak Nilsson
Karl Steen

CHALMERS
UNIVERSITY OF TECHNOLOGY

Department of Mechanical Engineering
Chalmers University of Technology
Gothenburg, Sweden 2026

How Micro-Geometry of Cutting Edges Influences Surface Integrity
An Experimental Study on the Effects of Cutting Edge Micro-Geometry and Its Influence on the Surface Integrity of Machined Surfaces
Isak Nilsson
Karl Steen

Supervisor: Erik Henrikson, GKN Aerospace
Examiner: Peter Krajnik, Department of Mechanical Engineering

Master's Thesis 2026
Mechanical Engineering
Chalmers University of Technology
SE-412 96 Gothenburg
Telephone +46 31 772 1000

Cover: Picture showing a scanned test surface, with a height magnified 3500%.

Typeset in LaTeX
Printed by Chalmers Reproservice
Gothenburg, Sweden 2026

How Micro-Geometry of Cutting Edges Influences Surface Integrity
An Experimental Study on the Effects of Cutting Edge Micro-Geometry and Its Influence on the Surface Integrity of Machined Components
Isak Nilsson
Karl Steen
Department of Mechanical Engineering
Chalmers University of Technology

Abstract

The aerospace industry relies heavily on the structural integrity of machined components. Even the smallest surface and subsurface defects can drastically reduce the components' fatigue life, possibly resulting in catastrophic failure. This thesis quantitatively evaluates the impact of cutting edge micro-geometry. Specifically, how edge radius and symmetry affect surface integrity during the machining of Ti-6Al-4V.

A fundamental experimental study has been conducted to investigate how changes in a cutting edge's sharpness and shape, its micro-geometry, affect the surface integrity of the machined part. A series of orthogonal cutting tests in Ti-6Al-4V was made to investigate the elementary relationship between cutting edge micro-geometry and surface integrity under different cutting conditions. The results are evaluated through regression analysis to statistically describe the relationships.

It was found that cutting tools with larger radii and waterfall-shaped edges strongly impact surface integrity, regardless of variations in cutting speed and depth of cut. Other surface integrity variables, however, do depend on cutting speed and depth of cut, not just on cutting edge micro-geometry.

Keywords: Aerospace, Machining, Surface Integrity, Experimental Study, Cutting edge micro-geometry, Characterization, Regression model.

Acknowledgements

We would like to extend our deepest appreciation to everyone who supported us throughout this thesis and made our time at GKN Aerospace such a rewarding experience.

A special and sincere thank you goes to our supervisor Erik Henrikson. We would also like to thank Alexander Thempo, Klas Nordh, and Stefan Cedergren, as we are incredibly grateful for your continuous guidance and support.

Finally, we would like to thank the wider team of project AeroCut who helped us along the way, answering our questions and ensuring our time was highly educational.

Isak Nilsson, Gothenburg, June 2026
Karl Steen, Gothenburg, June 2026

Acronyms

BUE Built-Up Edge
CAM Computer Aided Manufacturing
DOE Design of Experiments
ESA European Space Agency
LOM Light Optical Microscope
PSZ Primary Shear Zone
RISE Research Institute of Sweden
SI Surface Integrity
SSZ Secondary Shear Zone
TSZ Tertiary Shear Zone
WEDM Wire Electrical Discharge Machining
XRD X-Ray Diffraction

Nomenclature

Below is the nomenclature for parameters and variables that have been used throughout this thesis.

Parameters

S_γ	Distance between separation from rake face and ideal tool tip
S_α	Distance between separation from flank face and ideal tool tip
$\bar{S}$	Average cutting edge rounding
κ	Form factor of the cutting edge
Δ r	Profile flattening
φ	Apex angle
β	Wedge angle
α	Clearance angle
γ	Rake angle
S	Symmetry ratio
a_f	Depth of cut
v_c	Cutting velocity
p_{int}	The intersection point between the tools bisector line and the cutting edge profile.
D_α	Vertical distance from the intersection between the straight fitting line and the horizontal line through p_{int} to the cutting edge profile on the clearance side.
D_γ	Vertical distance from the intersection between the straight fitting line and the horizontal line through p_{int} to the cutting edge profile on the rake side.

Variables

σ_{res}	Residual stresses
σ_a	Standard deviation of amorphous layer thickness
σ_{td}	Standard deviation of total deformation
σ_{ad}	Standard deviation of adhered material
σ_{st}	Standard deviation of surface tearing
F_c	Cutting force
F_f	Feed force

Contents

List of Figures

List of Tables

1
Introduction

GKN Aerospace is one of the world's leading multi-technology aerospace suppliers. With 33 manufacturing locations in 12 countries, they serve over 90% of the aircraft and engine manufacturers [1]. GKN designs and manufactures innovative, smart aerospace systems and components. The technologies are used in a wide range, from the most commonly used civil aircraft to the world's most advanced 5th generation fighters and the Ariane orbital rockets used by European Space Agency (ESA).

To guarantee their duty life, critical aerospace parts must pass tight tolerances. These parts need to meet multiple criteria for surface integrity, with microstructural deformation among them. Microstructural deformation is an effect of the machining processes and is known as surface integrity. Numerous factors may impact the surface integrity of machined surfaces. This project will focus on one of these aspects. More specifically, the micro-geometry of the cutting edge. In detail, this includes the shape of the cutting edge, its symmetry, and size, as these have been shown to have a great influence on the surface quality, tool life, and dimensional accuracy [2] [3].

1.1 Industrial context

In the aerospace industry, many of the components have to endure harsh environments. Due to this, the materials used often have to have a high thermal fatigue resistance, with Ti-6Al-4V being one example [4]. However, the material properties of these materials are not without their problems, and the machining process introduces several interesting challenges. During cutting, we introduce severe thermomechanical loads at the tool-workpiece interface [5]. These loads affect the material and can result in several phenomena affecting the material. These include material drag, formation of amorphous layers, and adhered deposits from a Built-Up Edge (BUE) [6]. These microstructural deformations can severely impact the performance of the material, drastically reducing fatigue life, potentially risking lives if not caught in time.

Looking at historical events, we can see occasions where such alterations resulted in catastrophic failures. A specific example is the Delta Air Lines flight 1288, which experienced an uncontained engine failure during its take-off, ending two of the passengers' lives and seriously injuring two more [7]. After a thorough investigation, the National Transportation Safety Board found that the probable cause was as follows:

"The National Transportation Safety Board determines that the probable cause of this accident was the fracture of the left engine's front compressor fan hub, which resulted from the failure of Delta Air Lines' fluorescent penetrant inspection process to detect a detectable fatigue crack initiating from an area of ***altered microstructure that was created during the drilling process*** *by Volvo for Pratt & Whitney and that went undetected at the time of manufacture. Contributing to the accident was the lack of sufficient redundancy in the in-service inspection program."* [7]

This is a very graphic scenario where a fatigue crack could initiate from an altered microstructure formed during the drilling process. The crack grew due to the cyclic nature of the aircraft's workload and showcases the importance of staying on top of maintenance and repairs, but also to make sure that all parts align with manufacturing protocols.

To ensure that no passenger pays the ultimate price, it is crucial that the aerospace parts being manufactured meet strict surface integrity standards. These standards are demanding, and the machining industry is continually evolving, with new machining methods and tool geometries being developed. These new methods have to be approved and qualified. However, this is a time-consuming and very costly process [8].

To optimize production and reduce the reliance on physical testing, there is a strong industrial push towards predictive modeling, reducing the need for physical destructive testing. A critical, yet often oversimplified, variable needed to develop an accurate predictive model is the exact condition of the cutting tool. While macroscopic parameters like feed rate and cutting speed are easily controlled, the micro-geometry of the cutting edge could dictate the fundamental physics of the cut and therefore govern the ploughing effect, heat generation, and subsequent surface alteration.

Prior research has shown that measuring the micro-geometry of cutting edges is not an easy task, and Denkena and Biermann [3] have conducted an experiment showing the difficulties. Considering this, establishing a robust methodology for measuring cutting edge geometry is a critical prerequisite to define how the micro-geometrical variations translate into surface defects.

1.2 Project AeroCut

The thesis is part of a larger research project involving GKN Aerospace, Research Institute of Sweden (RISE), and Chalmers University of Technology [9]. The project has been granted funding to develop a prediction tool that can guide Computer Aided Manufacturing (CAM) engineers to predict surface integrity. The goal of the tool is to reduce the amount of destructive testing needed to examine surface integrity when introducing new cutting tools or processes. The primary thesis motivation is to aid AeroCut with both qualitative and quantitative input data that can be used to develop and validate the prediction tool.

1.3 Aim

The thesis aims to systematically study the effect that different cutting edge micro-geometry has on the workpiece surface integrity. In addition, the thesis aims to find a relation between different geometrical features of the cutting edge and the impact on the surface integrity. Another aim is to come up with a consistent, robust, and repeatable test method for these kinds of experiments that could be used for similar experiments in the future.

Guiding the work towards this aim are the following research questions:

RQ 1.1: How does cutting edge micro-geometry affect surface integrity?

RQ 1.2: Do the effects remain consistent across various cutting parameters?

RQ 2: How can a robust and repeatable experimental methodology for evaluating the effects of cutting edge micro-geometry on surface integrity be established?

RQ 3: How can various cutting edge micro-geometries be consistently and accurately characterized?

2

Technical Background

This chapter will discuss the fundamental technical knowledge necessary to understand the topic in this report.

2.1 Cutting edge micro-geometry

The cutting edge micro-geometry is the intersection of the tool's flank face and rake face, and it describes the actual geometry and profile of the cutting edge [10]. It is established that the shape of the cutting edge affects both machining and surface properties, but researchers are not in total agreement about what the influence actually looks like. Whyen et al. [2] present, by referencing the DIN 6582 standard, mainly three types of profiles for cutting edges: round, sharp, or chamfered. Additionally, asymmetry is introduced. This generates five types of cutting edges, but this thesis will only cover the analysis of ideal round, trumpet-shaped, and waterfall-shaped cutting edges, and they are described in Figure 2.2.

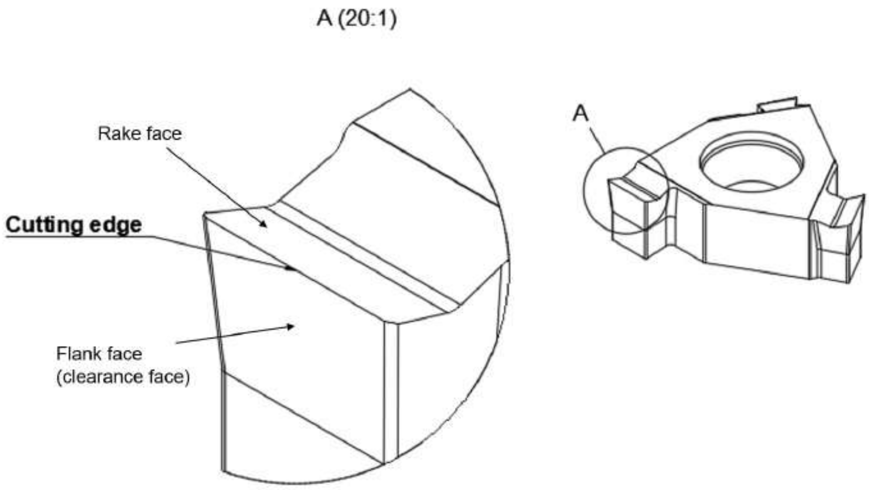

Figure 2.1: Description of cutting edge terminology used in this thesis.

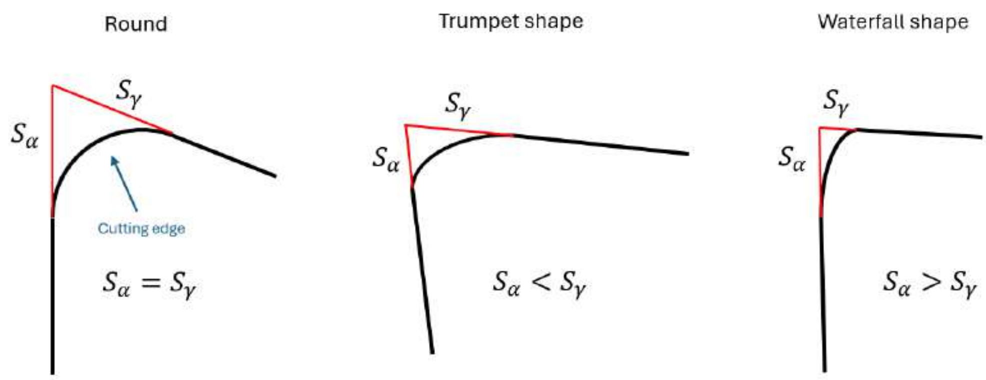

Figure 2.2: Illustration of cutting edge shapes.

2.2 Heat generation

A machining process is fundamentally a thermo-mechanical conversion where mechanical work is transformed into thermal energy through plastic deformation and friction. When analyzing the tool-workpiece interface, it is conventional to categorize the heat generation into three distinct regions, known as the Primary Shear Zone (PSZ), Secondary Shear Zone (SSZ), and Tertiary Shear Zone (TSZ). During machining, the three shear zones house large thermal build-ups and the majority of force [5]. These can be seen in Figure 2.5.

In the PSZ, the bulk material gets machined into chips. In doing so, the bulk material undergoes severe plastic deformation as it shears. The plastic flow occurs at very high strain rates, resulting in large thermal generation. The PSZ is therefore responsible for a large fraction of the total heat produced during cutting. In the SSZ, the chip rubs against the rake face. In doing so, it generates more heat due to the friction between the chip and tool. Finally, the TSZ forms along the tool's flank. Although less heat is generated than in the PSZ, it plays a critical role in the surface integrity of the final part, as this is the surface remaining after machining.

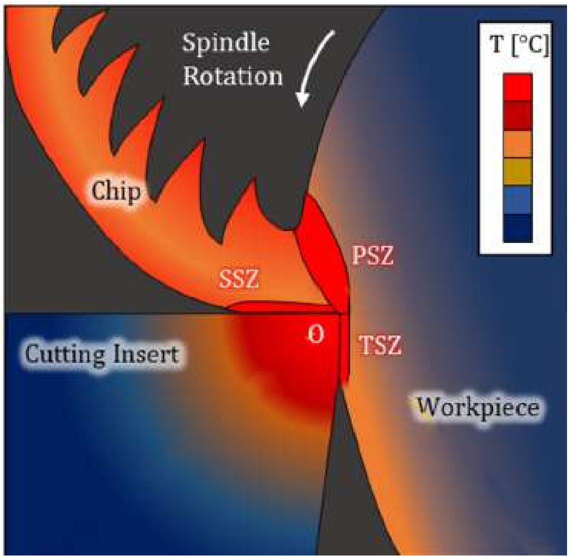

Figure 2.3: Thermal generation from machining and the corresponding shear zones [5]

2.3 Surface integrity

Surface integrity is a term that describes the metallurgical and topographical condition of a machined surface. When the tool interacts with the workpiece, the thermo-mechanical developed loads can significantly alter the surface layer relative to the bulk material, see Figure 2.4 [11]. When referring to surface integrity, several interrelated phenomena are included. Plastic deformation at the microstructural level may modify grain boundaries and influence subsurface hardness. Material flow around the cutting zone can lead to re-attached layers or smeared material, which may alter the surface. In addition, extreme localized temperature gradients can produce thermally affected zones, such as white layers. These areas are brittle and drastically reduce fatigue life.

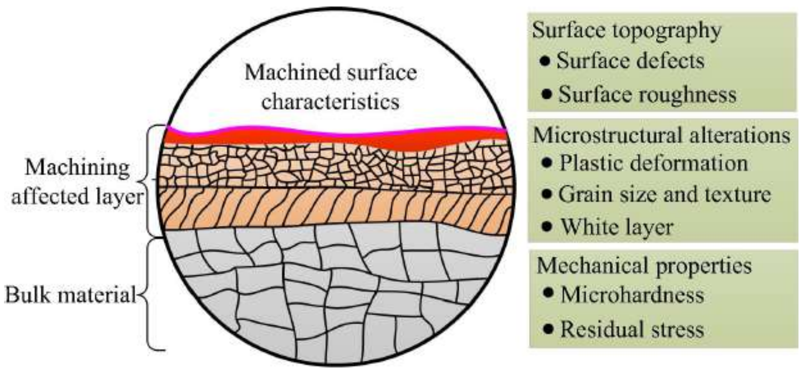

Figure 2.4: Illustration of how the surface integrity is affected during machining [11]

2.3.1 Plastic deformation

Plastic deformation is mainly driven by two factors, and these are thermal and mechanical interaction between the cutting tool and the workpiece [5][12]. In conventional machining of materials like steel, a large proportion of the generated heat dissipates through the chip. However, in contrast to steel and aluminum, the thermal conductivity of many materials used in aerospace, such as titanium and high-nickel alloys, is significantly lower [11]. Therefore, the thermal energy gets concentrated within the cutting tool and workpiece rather than dissipating. This results in the heat being confined to a very small volume at the cutting edge and in the nearest workpiece material. The result is a combination of high thermal and mechanical loads acting simultaneously on the material. As seen in Figure 2.5, this phenomenon occurs specifically in and around the TSZ, where the newly machined surface interacts with the tool flank. During cutting, the thermo-mechanical loads work synergis-

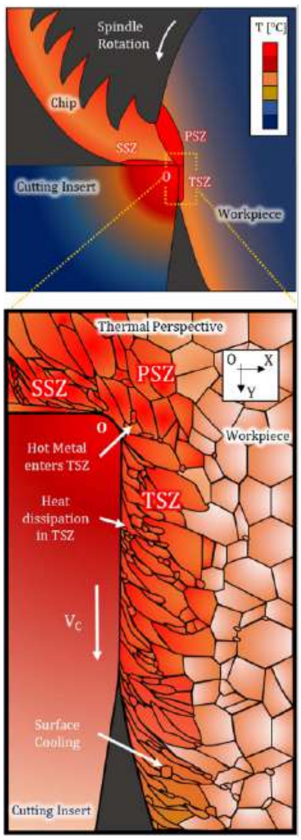

Figure 2.5: Illustration of thermal movement in the TSZ along the flank and workpiece interaction [5]

tically as a formation mechanism [12]. The forces generated in the interaction drag the material in the cutting direction. This can be seen as drag deformation in Figure 2.6. The plastic deformation itself also generates heat, thus intensifying the process. This results in thermal softening of the material. While thermal softening increases initial deformation, the rapid cooling that follows often leaves the machined surface in a state of high residual stress and increased hardness. It has been experimentally shown that the subsurface hardness of machined Ti-6Al-4V is higher than the bulk hardness due to the high density of dislocations generated during cutting [13].

Depending on the significance of the grain boundary distortions, the deformation is classed as a drag layer or an amorphous layer. The visual results of this and its implementation are shown in Figure 2.6.

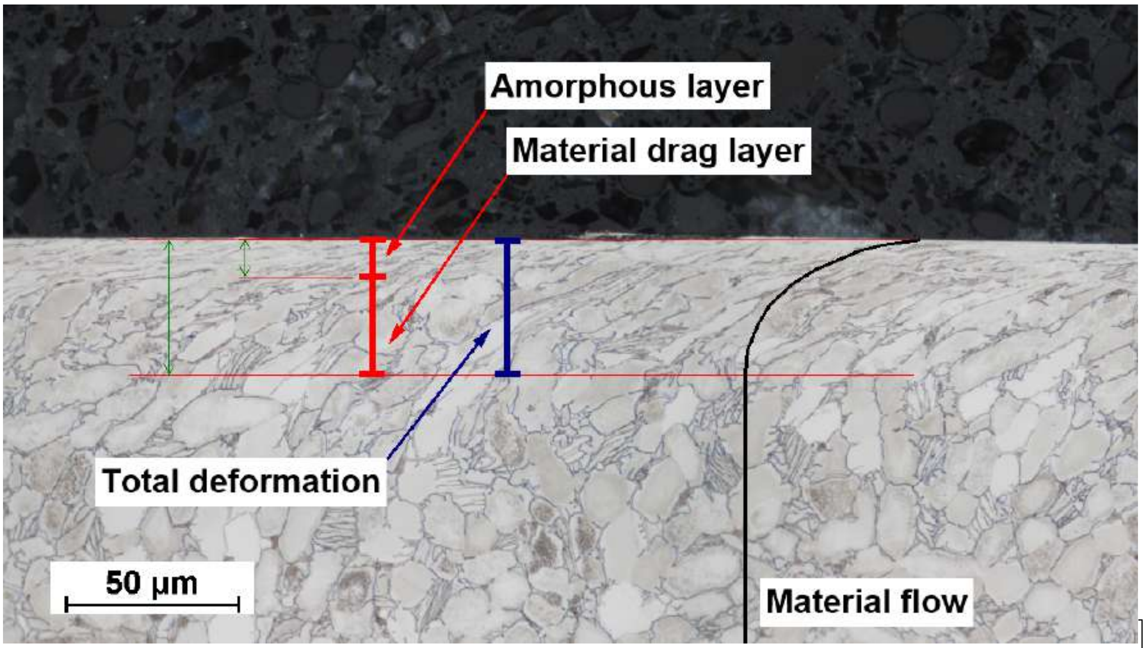

Figure 2.6: Microscopic picture of Ti-6Al-V4 taken with LOM. It illustrates total deformation and its constituents.

2.3.2 Adhered material and surface tearing

BUE is an accumulation of work material that adheres or welds itself to the tool face, causing a pile of material [6]. This results in a growing build-up, and eventually it becomes unstable and releases. The material then gets pushed along the underside of the tool, adhering to the workpiece surface, leaving a leap on the surface [6]. When the BUE releases, the tool pressure in combination with the heat makes it adhere to the surface. Surface tearing refers to the removal of material from a surface, which can happen when the adhesion between the tool and the surface is excessively strong, leading to the detachment of sections of the surface. This results in something known as a tear-out, disrupting the topography of the surface [6].

2.3.3 Residual stresses

Residual stresses are mechanical stresses that remain within the workpiece after the material has been under external loads from the cutting interaction [14][15][12]. Residual stresses are a result of the thermal and mechanical loads. Mechanical loads apply pressure on the workpiece that compresses the material, causing plastic deformation, thus resulting in compressive residual stresses. The thermal load, on the other hand, causes the material to expand. When the surface layer attempts to contract during cooling, the contraction is restricted by the underlying bulk material, resulting in tensile residual stresses.

2.4 WEDM

The manufacturing of high-precision cutting edges out of tungsten carbide can be very difficult. It is a material known for its hardness and durability, resulting in a hard-to-machine material [16]. WEDM is a non-conventional, well-established method to machine hard and high-precision surfaces. As the wire of a wire-WEDM passes through the workpiece, a current creates sparks, effectively vaporizing the workpiece [17]. The removal is very precise, and many passes can be done, removing as little as ≈ 2.5 µm in one pass. To reach higher tolerances, multiple passes can be done.

3

Related Work

This chapter will cover previous research papers related to the topic of this thesis and what their conclusions bring for this study. Table A.1 in the appendix summarises all relevant research papers and outlines the key findings derived from them.

3.1 Difficulties in characterizing micro-geometry

Denkena and Biermann [3] conducted an experiment where different researchers measured uncoated cemented carbide inserts with a contact stylus and optical measurement devices. The experiment revealed that the results differed by up to 48% when researchers measured the same radius, suggesting that a more robust method for measuring the cutting edge geometry is beneficial for defining changes in micro-geometry. As of now, there is no international standard on how to characterize cutting edge micro-geometry like there is for macro-geometry [18].

Wyen et al. [10] have made a detailed study on definitions of cutting edge micro-geometry. It covers the most common methods, highlights advantages and disadvantages, and then proceeds to suggest an improved method. There is an inconsistency in the results of studies that aim to map the influence of cutting edge micro-geometry on surface integrity. According to Wyen et al. [10], the root cause of this inconsistency lies in the characterization methods used to describe the micro-geometry. The general approach is to generate data points along the cutting edge profile using tactile or optical equipment. By picking different profiles along the edge from a 3D profile or averaging the generated data points, you have a shape ready for characterization. However, after this step, there is no general way to proceed.

3.2 Prior research on the effect of micro-geometry

Denkena and Biermann [3] experiment with different values of the "cutting edge rounding" and its effect on surface integrity in aluminum. Cutting edge rounding is a result of two parameters in the authors' definition of the cutting edge micro-geometry, which is described below and shown in 3.1.

- Cutting edge segments on rake face, denoted S_α. This is the distance from the separation point on the rake face and the tool tip of an ideal sharp cutting edge at the flank face and rake face.

- Cutting edge segments on flank face, denoted S_γ. This is the distance from the separation point on the rake face and the tool tip of an ideal sharp cutting edge at the flank face and rake face.
- Profile flattening, denoted Δr. This is the shortest distance between the ideal tool tip and the actual tip.
- Apex angle, denoted φ. This is the angle between the bisector, created from the angle between the rake face and flank face, and a hypothetical line between Δr and the ideal tool tip.

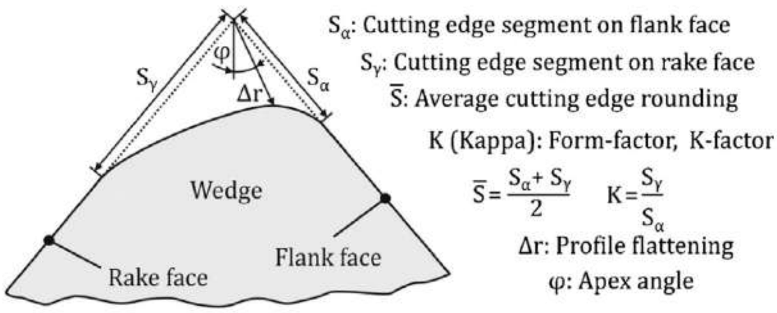

Figure 3.1: Characterization of cutting edge micro-geometry [3]

Their experiments revealed that cutting edge rounding $\bar{S}$ affects surface roughness R_z. Larger cutting edge rounding, achieved through increasing S_α and S_γ, resulted in higher values of R_z.

Gertsenmeyer et al. [19] analyzed how the cutting edge micro-geometry influenced cutting forces and heat generation by different values of κ. By building a 3D FEM model in ABAQUS using Denkena and Biermann's definition [3], the project aimed to study the induced surface integrity. Their results showed a trend where $\kappa < 1$ resulted in larger cutting forces. Process forces have then been shown to impact surface integrity, more specifically micro-hardness, in a study from Kishway et al. [20]. However, the study also showed that $\kappa > 1$ could contribute to higher localised temperature [19].

One of the other project participants in AeroCut has performed simulations on how different ratios between S_α and S_γ influence cutting force and feed force [21]. Five different micro-geometries were tested with $\kappa = 0.5$, 1, and 2; see Figure 3.2 for images. The findings were that $\kappa < 1$ resulted in higher process forces than when $\kappa > 1$. This aligns with the findings by Gertsenmeyer et al. [19]. Furthermore, the simulation experiments revealed that increasing the magnitude of S_γ and S_α, while maintaining the same κ, increases the reactive forces during the process [21]. As stated before, the reactive forces in a machining process influence the surface integrity [20]. The material used in the simulation was Ti-6Al-4V.

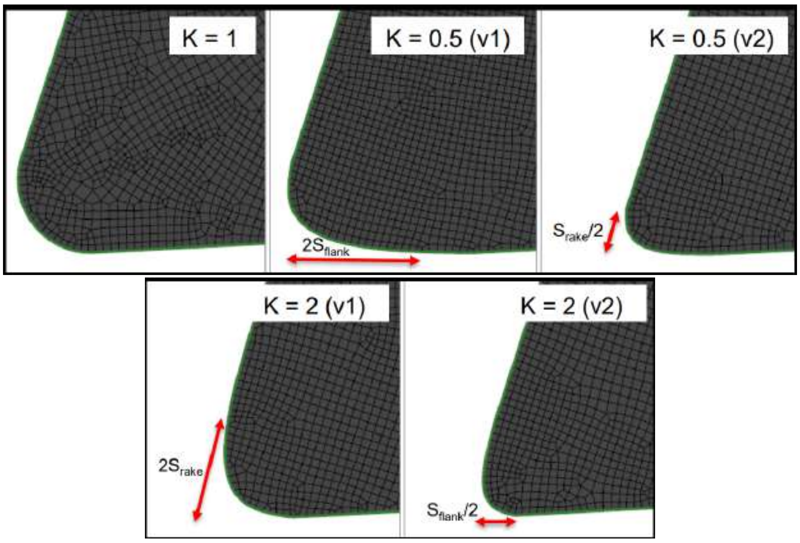

Figure 3.2: Images of the different tools used in the simulation by A. S. Ertürk [21]

The cutting edge radius has been shown as a critical geometric parameter in machining processes and becomes particularly significant in precision cutting. Early studies demonstrated that an increased cutting edge radius leads to higher cutting forces due to a number of reasons [22]. An interesting finding in the experiment by D. J. Waldorf et al. [22] was that a larger edge radius significantly increased the cutting force due to build-up on the cutting edge. Additionally, the ploughing force also increased when the feed rate was below the size of the edge radius.

Pérez-Salinas [23] studied the effect of how different edge radii affect the surface integrity and residual stresses. The experiments were performed on orthogonal cutting tests carried out on a CMZ TC25BTY 4-axis CNC lathe. Edge radii from 5 to 15 µm were tested. The results showed that the depth of the stresses reached 0.4 mm and that the 5-15 µm radius made the least damage to the surface integrity.

Hu et al. [24] have made efforts to create an enhanced numerical model to capture the plastic deformation induced by the radius during the machining of Ti-6Al-4V titanium alloy. The model employs finite element simulations, and one of the findings was that the tool with the larger radius generated deeper deformation. Their study compared two different radii, 16 µm and 30 µm, with the induced deformation layer thickness ranging from 90 to 130 µm.

3.3 Improved method for characterizing the micro-geometry of cutting edges

An improved method to characterize cutting edges is suggested in the same paper from Wyen et. al. [10]. Usually, a fitting area is manually chosen to represent the micro-geometry, and this area, often a part of the tip of the cutting edge profile, is then characterized by a fitting algorithm. The authors explain that the manual decision on where the macro-geometry transitions to micro-geometry is an uncertainty that affects the calculated geometry, and they highlight the need for a characterization method that is independent of that transition.

The method that Wyen et. al. [10] created iteratively finds the correct fitting region, and then uses a least-squares fitting algorithm with the points inside the found region. Figure 3.3 illustrates the procedure of finding the fitting area that is used to characterize the micro-geometry.

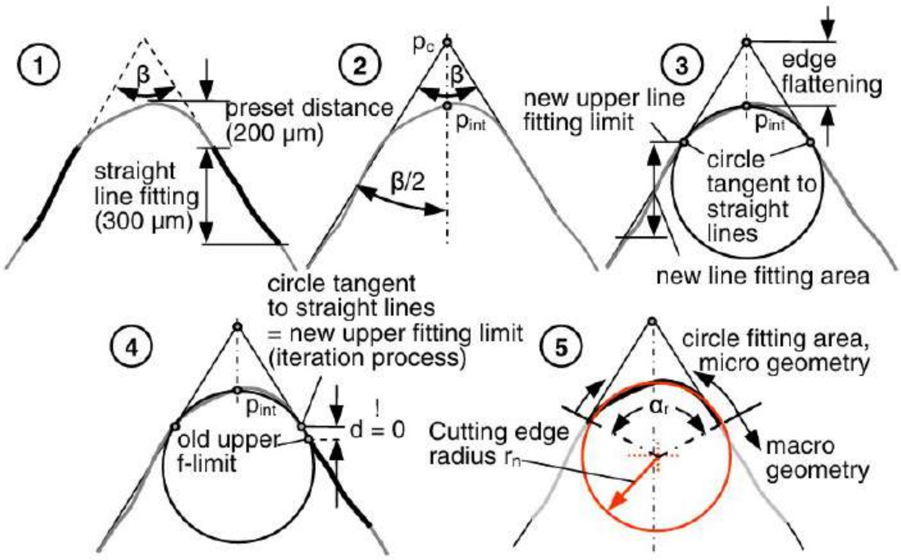

Figure 3.3: Illustration from *A new method for the characterization of rounded edges* by Wyen et. al. [10]. Showing the step-by-step procedure for finding the fitting area.

The first step is to decide on an initial guess for the length and location of the data points that later will form two straight fitting lines for the rake face and clearance face, respectively. The preset distance should represent the expected vertical distance from the tool tip to the transition point between macro-geometry and micro-geometry. It will be the point where the set of data points that estimates the fitting line begins. The fitting length is the vertical length for the space that defines what data points should be used in order to create the straight fitting lines later. If a longer distance is chosen, more points are used to estimate the fitting lines. The lines should be chosen in such a way that it corresponds to the maximum uncut chip thickness that the tool will be used for.

The second step is to create a best-fitted line on each side, and these lines cross each other at p_c. The bisector of the two fitting lines intersects with the tool profile at p_{int}.

The third step involves drawing a circle that crosses p_{int} and is tangent to both fitting lines. The points where the circle is tangent to the fitting lines become the new upper limits instead of the initial preset distance.

In the fourth step, the distance between the old upper limit and the new upper limit is measured. Unless it is larger than a small number, which the user defines, the procedure is done again from step 2. That is to say, creating new fitting lines based on the new upper limit and creating a new circle. When the distance between the new preset distance and the previous distance is close to zero, the iterations stop. The current tangent points on the circle are where the micro-geometry begins.

The fifth step is to create a circle using a least-squares algorithm on the data points within the micro-geometry. The radius of this circle is the estimated tool radius. This circle does neither need to touch the fitting lines nor have its center located at the bisector line.

The sixth and final step is to evaluate the asymmetry of the profile. A horizontal line is drawn through p_{int} to the points where it intersects with the straight fitting lines. From these intersection points, a vertical line is drawn until it reaches the tool profile. The distances of these vertical lines are called D_α and D_γ. The asymmetry of the cutting edge is defined according to equation 3.1 [10].

$$S = \frac{D_\gamma}{D_\alpha} \tag{3.1}$$

Figure 3.4 illustrates how the dividend and divisor are retrieved.

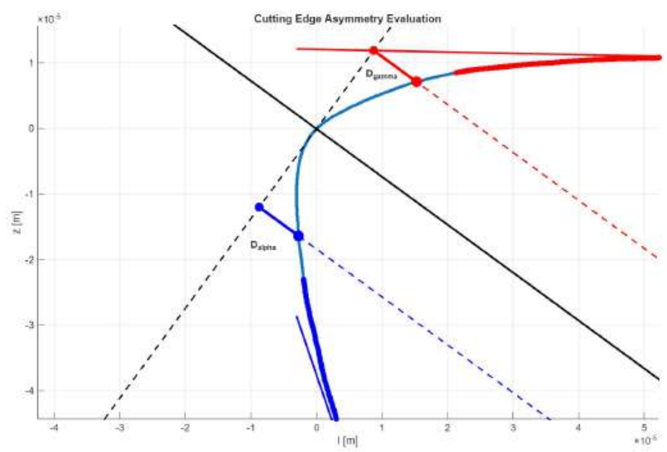

Figure 3.4: Illustration of D_α and D_γ in a MATLAB plot.

3.4 Previous research on the impact of cutting speed

One of the most dominant factors directly affecting the surface integrity is the cutting speed [2][4]. As shown by Ortiz de Zárate et al. [2], the surface roughness alters in both the transversal and longitudinal direction of cutting when the cutting speed changes. In their paper, the surface quality increased while R_z and R_a both decreased when the cutting speed was changed from 2.5 m/min to 7.0 m/min. However, the temperature during the process increased with this change. [4].

3.5 Effect of cutting edge radius on residual stresses

In their research paper about cutting edge geometries, Denkena and Biermann summarize multiple articles that have investigated the effect of cutting edge micro-geometry on surface integrity in steel [3]. One finding was that large tool radii lead to more compressive residual stresses than smaller radii. The authors continue by emphasizing that an increasing extent of material that is pressed into the work surface while cutting with rounded cutting edges is the reason behind this. Moreover, they found that residual stresses increase with tool radius until the cutting edge rounding $\bar{S}$, described in Figure 3.1, reaches the same size as the depth of cut. The residual stresses decrease with increased radius after that point.

4
Methods

Conducting these experiments has required a lot of different steps. All of these are equally important to follow the aim of the thesis: to systematically study the effect of micro-geometries and to suggest a robust, repeatable experiment setup. This chapter will describe these steps in detail.

4.1 Delimitations

In order to limit the scope of the study, environmental and machining parameters such as lubrication, tooling material, part material, the initial microstructure, and machine setup will be consistent.

Although cutting edge micro-geometries are small and might change slightly during operations due to wear [25], the study does not aim to study the prolonged use of the cutting edges.

This study will cover the fundamentals of metal cutting and be based on orthogonal cutting, although many industrial implementations are oblique. The modeling and design of cutting edges will therefore be from a two-dimensional perspective.

Ti-6Al-4V will be the studied material. It is commonly used in the aerospace industry because of its high strength, fatigue resistance, corrosion resistance, and thermal properties [26]. The preparation and images of the material can be found in Appendix B.

4.2 Design of cutting edge

Based on the overall findings in previous research and the literature review, a method for designing the cutting edges has been considered. The literature review resulted in the decision to analyze two geometrical parameters, cutting radius and symmetry. It is important that the method of designing the cutting edges enables isolated control over each chosen input parameter in the experiment. To isolate changes in symmetry and radius, the micro-geometry will be drawn with a cone shape that is tangent to the rake face and flank face at the separation points. Both the radius and symmetry can be altered by changing the distances S_α and S_γ. When the desired geometry is set, the cone needs to be replaced by several small radii that are tangent to each other. This step was necessary to make the design compatible with the CAM software for the WEDM.

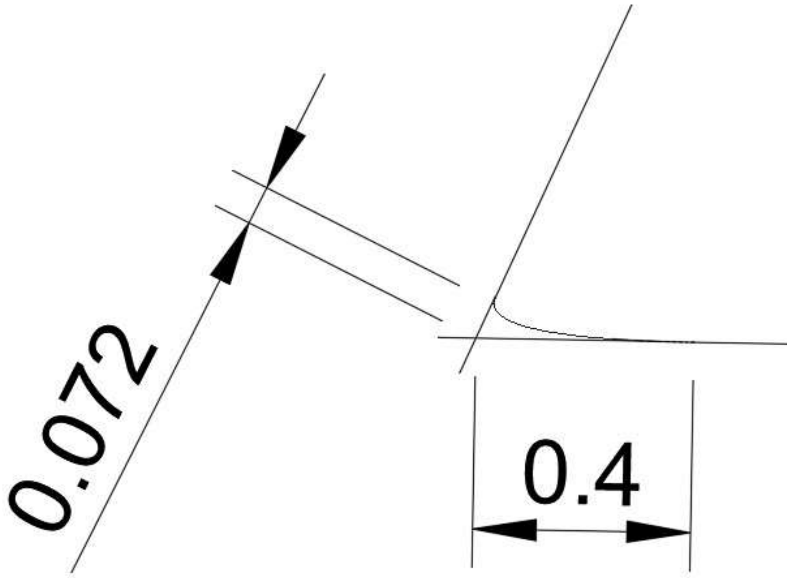

Figure 4.1: Sketch of cutting edge in Autodesk Fusion. The dimensions in the drawing are S_α and S_γ

To reduce the risk of tool vibrations caused by feed forces, the tools are designed in such a way that the cutting edge is placed exactly beneath the centre of the tool holder. More specifically, the new cutting edge is rotated in comparison to the original one. This removes any potential torque on the spindle that could cause vibrations, which could damage the test results.

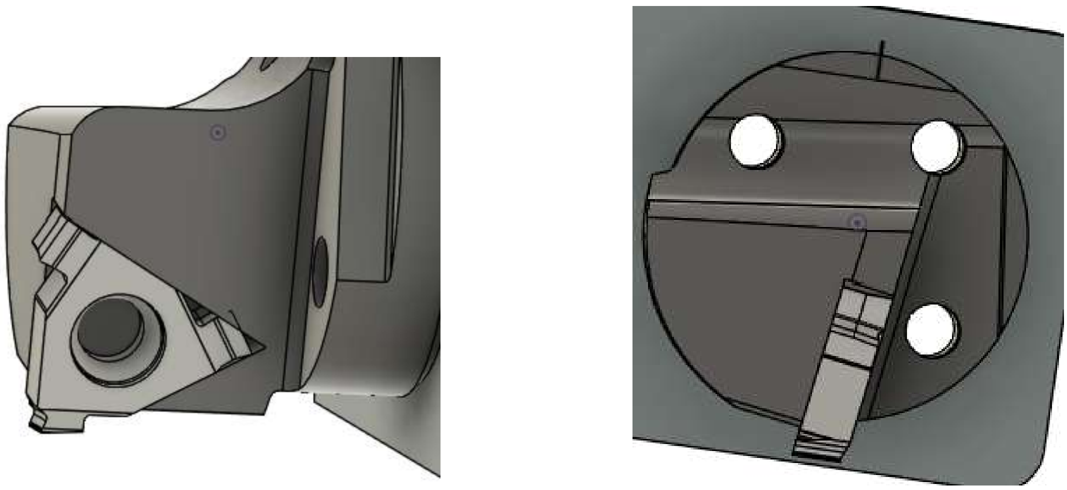

Figure 4.2: Images from Autodesk Fusion showing how the cutting insert is positioned on the tool holder.

4.3 Manufacturing of cutting edges

The cutting edges were cut out of Sandvik 254LG-22CC01-415 1135 carbide inserts with WEDM. To produce a smooth surface, seven passes were done. The cutting edge was placed in a cutting fixture in the WEDM that has been designed for this specific experiment. This allowed an accurate and consistent positioning of the cutting edge. To enable current flow through the tool holder, the coating was removed from the contact surfaces between the screws and the tool holder by sandblasting.

A cut, which can be seen in Figure 4.3, was made on the tool holder while manufacturing the cutting edges in WEDM. This cut was designed to be parallel with the new cutting edge and later served as a reference when aligning the spindle in the CNC machine.

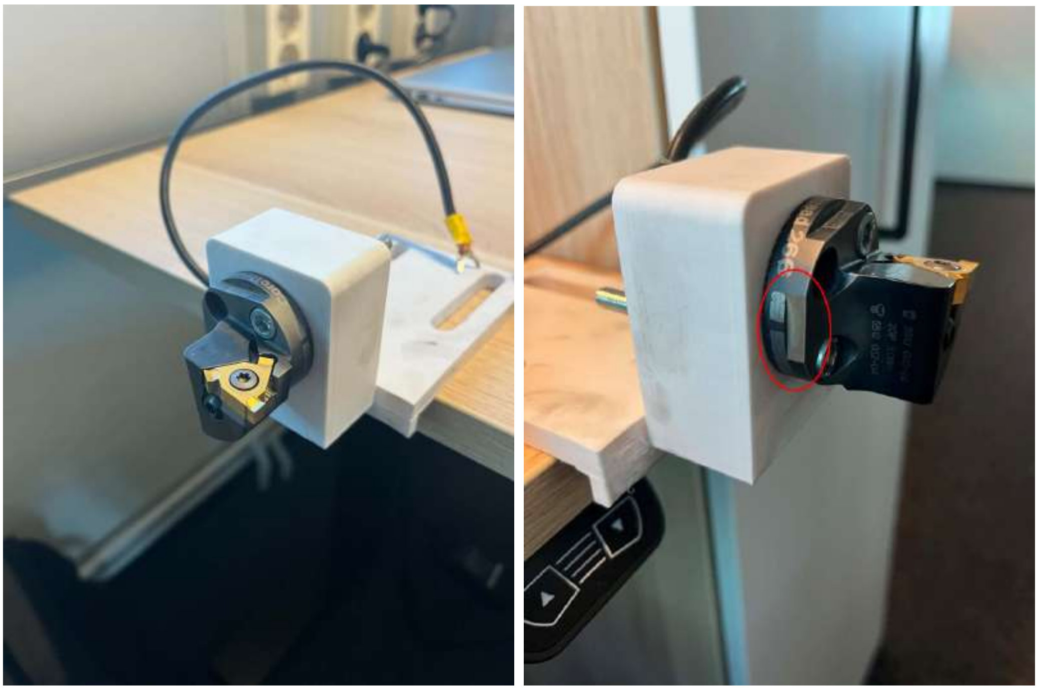

Figure 4.3: Cutting fixture made out of PLA. The fabricated cut on the tool holder is marked in red.

4.4 Measuring the micro-geometry

After the literature review, it was decided to follow the characterization method of Wyen et al. [10]. By using their iteration method, one can be sure that they always find the same transition between macro-geometry and micro-geometry. To execute this method, a MATLAB program was developed that uses data points from an Alicona Edgemaster as input. Alicona EdgeMaster is a specialized piece of equipment used to measure cutting edges using focus-variation and can produce high-resolution spatial data [27].

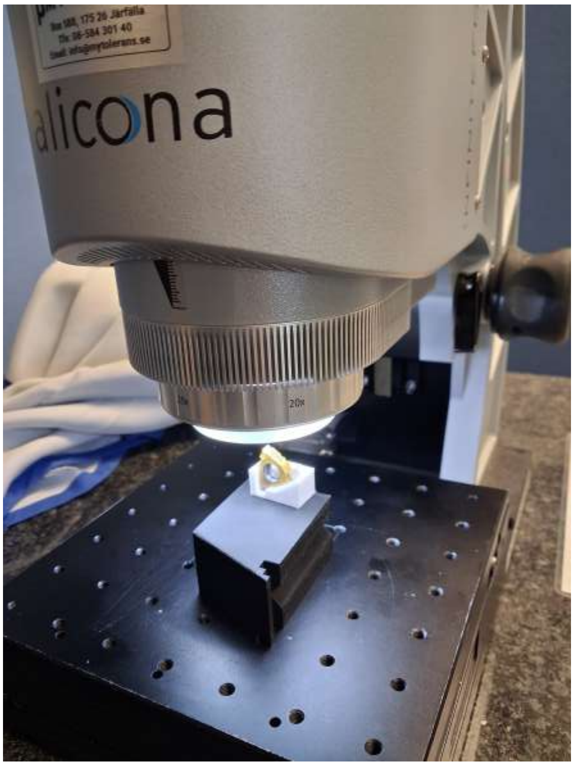

Figure 4.4: Alicona EdgeMaster measuring a cutting edge.

Data points, wedge angle, clearance angle, and rake angle were retrieved from the Alicona Edgemaster and then used as input in the MATLAB program. The program finds the intersection between the macro-geometry and the micro-geometry, using the method by Wyen et al. [10], and returns a best-fitted radius for the cutting edge. It also returns the symmetry ratio S, which is attained by following the author's suggested way to characterize the symmetry of cutting edges. A ratio above 1 indicates a waterfall-shaped edge, and a ratio below 1 indicates a trumpet-shaped cutting edge. All shapes are illustrated in Figure 2.2. Furthermore, a coefficient of determination R^2 for the fitted profile is calculated with the following equation:

$$R^2 = \frac{SS_{\text{reg}}}{SS_{\text{tot}}} = \frac{\sum_{i=1}^{n}(\hat{r}_i - \bar{r})^2}{\sum_{i=1}^{n}(r_i - \bar{r})^2} \tag{4.1}$$

where $\bar{r}$ is the mean radius of the cutting edge, r_i is the observed radius and $\hat{r}_i$ is the predicted radius.

The MATLAB program was also used in the process of designing the geometry of the cutting edges. A Python add-in for Autodesk Fusion was created that generated data points along the micro-geometry, similar to how the Alicona Edgemaster generates data points. These data points could then be evaluated in the MATLAB program, and if the output gave a radius and symmetry value that was not as intended, the distances S_α and S_γ were altered. This was an iterative process until the desired geometry was achieved.

4.5 Design of test pieces

For the analysis of the micro-geometry to be valid, the deformation at the studied cross-section needs to be plain strain deformation. Pednekar et al. [28] have done research through simulations which showed that a ratio between depth of cut and workpiece width of 1:20, given that the cutting tool is wider than the workpiece, gives plane strain deformation through more than 90% of the width of the workpiece. This ratio was taken into account when deciding on the test piece geometry. Furthermore, simulations of orthogonal cutting by Ertürk [21] showed that process forces reach a steady state after 0.5 mm of engaged cut.

The geometry of the test pieces can be seen in Fig 4.5. It is a 3 mm thick sheet that is approximately 25 mm long. The corner where the cut is initiated is chamfered in order to secure a smooth entry. The bottom corners are chamfered to better fit the machine vise that holds the test piece in place during the cutting procedure. All test pieces are made from Ti-6Al-4V with a hardness of 319 HV0.3.

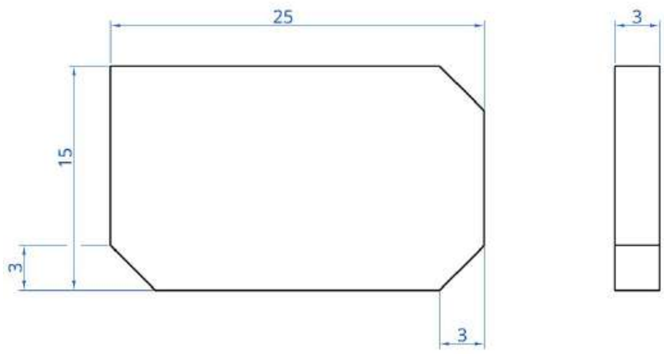

Figure 4.5: Drawing of test piece used in experiments, dimensions in millimeters. Cutting direction from right to left.

4.6 Experimental setup

All experimental trials were conducted on a GROB G350, located at Industrigymnasiet at GKN Trollhättan. As illustrated in Figure 4.6, this machine features a horizontal spindle configuration. To accurately replicate the mechanics of orthogonal cutting, the experiments required a strictly linear tool path. The motion was restricted to the primary translational axes, X, Y, or Z, to minimize overall complexity. GROB also specifies that the maximum rapid traverse speeds for the X, Y, and Z axes are 70, 45, and 90 m/min, respectively [29].

The experimental setup focused on minimizing compliance. Therefore, the Z-axis was selected as the primary feed direction. The specific machine spindle utilized for this study is equipped with an HSK-A 63 spindle interface. This interface does not offer a consistent clamping position. Therefore, the tooling position was clocked in between every test piece to ensure consistent tool positioning.

Figure 4.6: A illustration showing the layout of a GROB G350 [29]

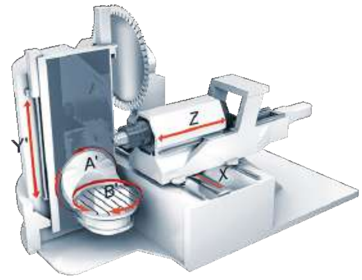

Figure 4.7: Definition of the machine coordinate system (MCS) for the GROB G350 5-axis machining center. [29]

4.6.1 Tool holders and adapters

To interface with the machine's HSK-A63 spindle, a Sandvik Coromant HT06-40-SL40N-110 HSK-to-SL adapter was used, as shown in Figure 4.9. The modular interface provided a rigid connection and enabled rapid interchange of cutting inserts while maintaining a constant tool overhang and stiffness, thereby ensuring that differences in surface integrity could be attributed to the cutting edge micro-geometry.

4.6.2 Test piece setup and sensors

A machine vise was designed and manufactured to hold the test piece in place during machining. This vise was mounted on a Kistler plate, which was in turn attached to the machine table. A white rag was placed behind the setup to catch the chip and prevent it from getting lost. The Kistler plate measures reactive forces in the X-direction and Z-direction and sends the signals through a Multichannel Charge Amplifier type 5070. Then, a data acquisition module for DynoWare, the software used to handle and view the data, converts the signals to digital data.

Figure 4.8: Photograph of how the test piece, machine vise, and Kistler sensor are positioned.

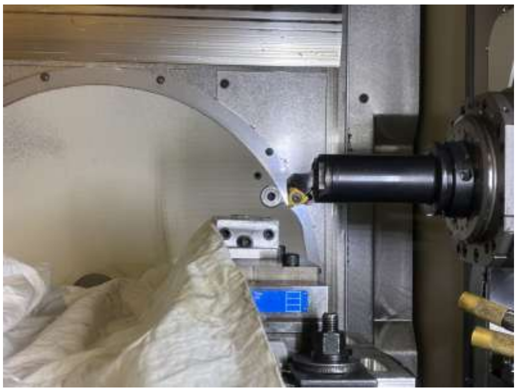

Figure 4.9: Photograph of entire experiment setup.

4.7 Design of experiments

Even though the thesis aims to discover patterns between cutting edge micro-geometry and surface integrity, more parameters were taken into account when setting up the design of experiments. By doing this, it was possible to see whether any potential patterns only appeared under certain cutting conditions.

The studied radii of the cutting edges ranged from 5 µm to 35 µm. These values are based on tools used in the aerospace manufacturing industry. The range of the symmetry, denoted S, was based on the values of κ that appeared in research papers during the literature review. The chosen range for S was set to 0.25-4. A value for S below 1 is what generates a waterfall shape, and a value above 1 generates a trumpet shape. The cutting speeds were determined to be between 2.5 and 10 m/min, and the cutting depth was 0.05-0.10 mm. The values of the parameters are based on previous experiments, as they provide a good baseline to orthogonal cutting [2][23].

Furthermore, the information above was put into MODDE, a software for managing DOE, in order to get the final DOE. The software assumes that the parameters increase linearly in their respective range, but that is not the case for the symmetry value, which has a middle value of 1. To adjust for this, the symmetry value was represented by logarithmic values with a base of 2. Equations 4.2 and 4.3 demonstrates how this is done:

$$-2 = \log_2(0.25) \tag{4.2}$$

$$2 = \log_2(4) \tag{4.3}$$

With logarithmic values, MODDE is allowed to increase the symmetry value linearly from -2 to 2.

A full factorial design with three center points has been used in this project, a design that investigates all combinations of variable endpoints and adds three experiments with the middle values in the variable range. Factorial designs are often used in experiments that take into account several factors, where it is necessary to study the interaction effect of factors on the response [30].

Table 4.1 presents the suggested DOE. It was expected that the cutting edges would not have exactly the desired micro-geometry after WEDM. After analyzing the finished cutting edges in the MATLAB program, the DOE was updated with the actual radii and symmetry values.

Table 4.1: Initial DOE generated from MODDE. *Symmetry values are logarithmic with a base of 2.

Exp. No.	Radius [µm]	S*	v_c[m/min]	a_f[mm]
1	5	-2	2.50	0.05
2	35	-2	2.50	0.05
3	5	2	2.50	0.05
4	35	2	2.50	0.05
5	5	-2	10.00	0.05
6	35	-2	10.00	0.05
7	5	2	10.00	0.05
8	35	2	10.00	0.05
9	5	-2	2.50	0.10
10	35	-2	2.50	0.10
11	5	2	2.50	0.10
12	35	2	2.50	0.10
13	5	-2	10.00	0.10
14	35	-2	10.00	0.10
15	5	2	10.00	0.10
16	35	2	10.00	0.10
17	20	0	6.25	0.75
18	20	0	6.25	0.75
19	20	0	6.25	0.75

Two sets of additional experiments were also planned. These are not directly tied to the thesis question, but still valuable for the AeroCut project, and all of the additional experiments have been analyzed in the same way as the main ones. The first additional set of experiments aimed to investigate the difference in surface integrity between a lubricated surface and tool and a dry surface and tool. In the original experiments, all surfaces and cutting edges were lubricated with a few droplets of oil. The second batch of additional experiments aimed to investigate how cuts with no cutting depth affect surface integrity, something that is common in machining processes such as broaching.

Table 4.2: Additional experiments under dry cutting conditions. *Symmetry values are logarithmic with a base of 2.

Exp. No.	Radius [µm]	S*	v_c[m/min]	a_f[mm]
1	20	1	6.25	0.08
2	35	-2	2.50	0.05
3	5	2	2.50	0.05
4	35	-2	2.50	0.10
5	5	2	2.50	0.10

Table 4.3: Additional experiments with no depth of cut. *Symmetry values are logarithmic with a base of 2.

Exp. No.	Radius [µm]	S*	v_c[m/min]	a_f[mm]
1	20	1	2.50	0.00
2	5	-2	2.50	0.00
3	35	2	2.50	0.00
4	5	-2	2.50	0.00
5	35	2	2.50	0.00

4.8 Execution of experiments

Each round of experiments began by inserting the right cutting tool in the tool holder. The spindle was locked in a position where the cutting edge was horizontal with the help of the fabricated cut on the tool holder. A touch probe was used to make sure that the surface of the test piece was parallel to the cutting direction. After this, clearance cuts were performed until a fully intact chip was produced, meaning that the whole surface area of the test piece had been cut. This was done to prepare for an orthogonal cut. Before the real cut was executed, a dial indicator was used to set a zero, and a drop of oil was added to the test piece and tool.

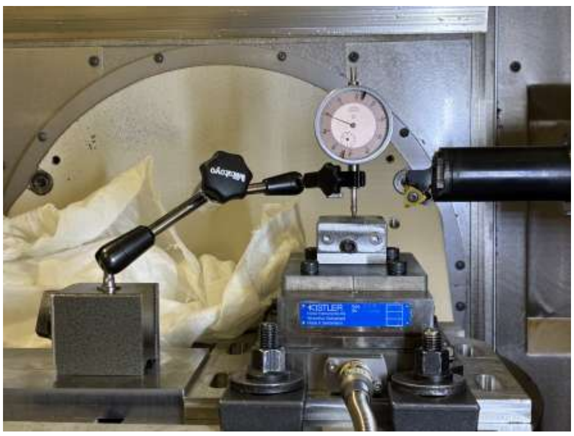

Figure 4.10: Photograph showing the dial indicator in use during one of the experiments.

After the cut was performed, the chip was collected and stored in a zip bag. The removed material thickness was then measured by placing the dial indicator back on the same spot, and the measurement was written down. The data plot of the forces was collected from DynoWare.

4.9 Sample preparation

All samples were cut in transversal or longitudinal directions. The transversal direction is defined as the perpendicular surface to the cutting direction. The longitudinal cutting direction is defined as the cut along the direction of cut, as seen in Figure 4.11

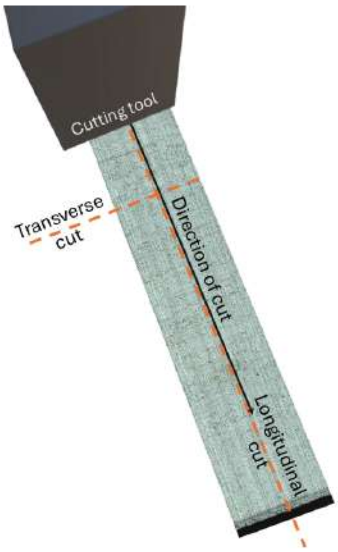

Figure 4.11: Illustration of how the cutting direction relates to cut-up definitions (not to scale).

Metallographic sample preparation of the test results was carried out in accordance with ASTM E3 – Standard Guide for Preparation of Metallographic Specimens. The objective of the preparation procedure was to obtain a surface with no alterations from the sample preparation that would be suitable for reliable microstructural examination. Specimens were sectioned from the bulk material using an abrasive cut wheel to minimize thermal and mechanical damage.

All samples were mounted, polished and then etched in accordance with ASTM E407 – Standard Practice for Microetching Metals and Alloys. This reveals the microstructure and deformation from the experimental stage to allow for the LOM analysis.

4.10 Description of analyzes

All test pieces have gone through several steps of analysis, both by the thesis group and by RISE. This subchapter aims to describe how each analysis was done.

4.10.1 Data handling of forces

All force measurements from the experiments have been analyzed in another MATLAB program that has been developed for the purpose of this thesis. The program plots the force profiles and allows the user to choose a segment where the process forces seem to have been in steady state. From this segment, an average force for each direction is derived.

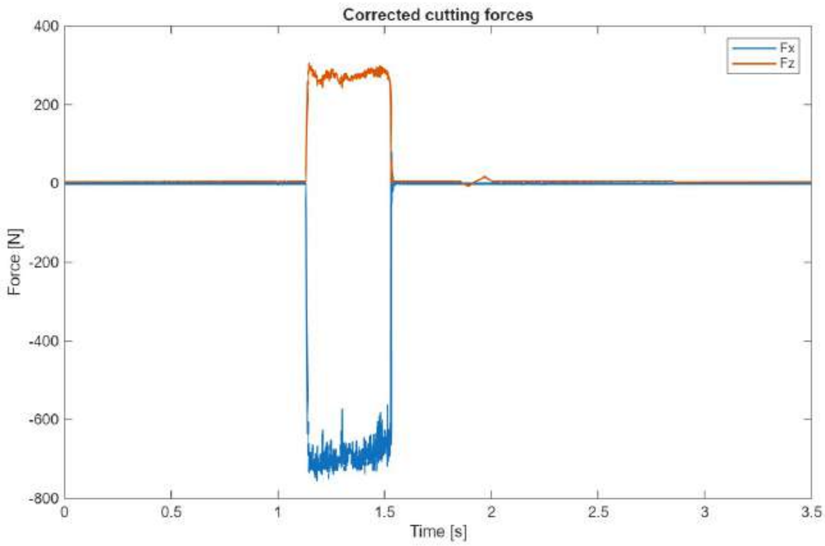

Figure 4.12: MATLAB plot of process forces captured during an experiment.

4.10.2 Surface analysis

All test pieces were cleaned, and then the machined surface was analyzed in a Keyence VK-X3000, a laser scanning microscope, with the laser confocal scanning method.

Images taken with the 5X objective were stitched together to generate a visual overview of the whole surface. One image of the exit zone was taken for each sample with the 20X objective. Finally, six different images were captured with the 50X objective. These were randomly selected over the machined surface. In each of these pictures, the amount of adhered material and the amount of material that has been removed by surface tearing have been analyzed in the Keyence software MultiFile-Analyzer.

A piece of adhered material was characterized as a piece of the surface that was elevated at least 0.2 µm above the mean surface. Furthermore, it needed to have a larger area than 5 μm^2. An example of areas that fulfill these requirements is marked in pink in Figure 4.13. As seen in the figure, many of these areas are very long and narrow, which is not common for adhered material. These appear due to the surface being wave-shaped and not entirely flat. To remove these false areas, a shape factor was introduced. If the longest horizontal distance within a marked area divided by the longest vertical distance was larger than 0.3, it was characterized as an adhered piece of material. The same procedure was performed to analyze surface tearing, but instead of looking for increasing height, the difference in depth was analyzed with the same criteria. An average of the number of adhered pieces of material and the number of surface tears was derived from the six pictures in order to estimate the whole machined surface. To quickly validate the method, the confidence interval

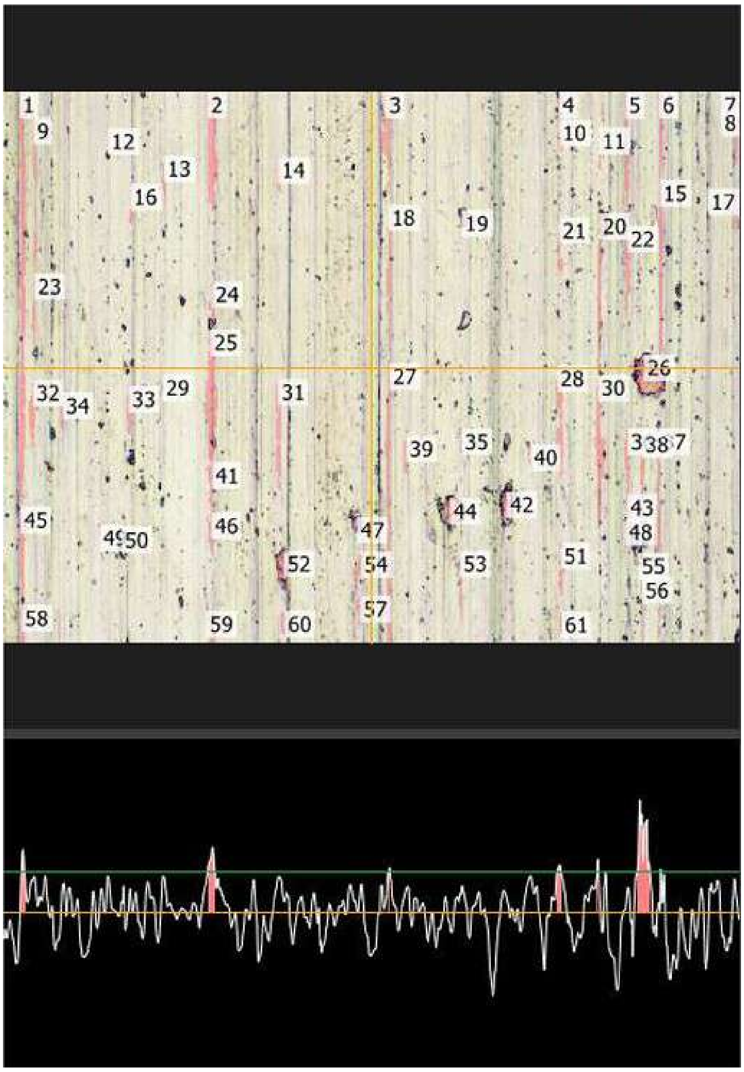

Figure 4.13: Image from the analysis tool. The graph represents the profile of the surface at a given horizontal line. The orange line in the graph represents the mean surface level, and the green line is set at 0.2 µm. The areas marked pink are areas that fulfil the requirements.

was derived based on the mean and standard deviation. With a confidence level of 95%, the following equation is used to calculate the interval [31]:

$$CI_{95\%} = \bar{x} \pm 2.571 \frac{s}{\sqrt{6}} \tag{4.4}$$

4.10.3 Analysis of microstructural deformation

The analysis of the grain structure was conducted through microstructural examination of the machined surfaces and the subsurface. The purpose of the etched samples was to identify metallographical changes caused by the thermo-mechanical loads developed during the machining. More specifically, finding grain elongation, grain boundary distortion, and plastic deformation. To visually analyze all metallographical changes, the samples were photographed using an LOM with the 500X magnification. Similar to the surface analysis in section 4.10.2, six different locations were chosen randomly and measured. Each location within a sample was then analyzed based on depth of distortion and type of deformation (drag deformation and amorphous layer). Mean values and standard deviation were calculated for each sample based on the six measurements.

4.10.4 Analysis of residual stresses

RISE has been doing X-Ray Diffraction (XRD) analysis on the test pieces to study the residual stresses. The surface of all samples has been analyzed both in the longitudinal direction and in the transversal direction, where longitudinal is along the cutting direction and transversal is perpendicular to the cutting direction. XRD is a non-destructive method commonly used to measure residual stresses in materials by analyzing changes in crystal lattice spacing [32].

4.10.5 Regression analysis

A regression analysis were made in MODDE that mathematically explains the effect each input variable had on the surface integrity parameters. Due to the experimental design being a two-level factorial, it is possible to explain the effects using linear coefficients and interaction terms [33]. Interaction terms become necessary when two variables combined have a different effect on the response compared to the effect that they both have individually. Equation 4.5 is an example of how the result of a linear regression analysis can look like. Y_i is the response that is being investigated, and in the case of this thesis, it could for example be residual stresses. X_i are the variables, which in this case are radius, symmetry, depth of cut, and cutting speed. All β-coefficients describe how much an increase in their respective variable affects Y_i, and ε is an error term.

$$Y_i = \beta_0 + \beta_1 X_{1,i} + \beta_2 X_{2,i} + \beta_3 X_{4,i} + \beta_4 X_{3,i} + \varepsilon \quad (4.5)$$

If an interaction term is used to describe the model, a coefficient for the combination alone will be presented. A positive interaction coefficient would mean that the combined effect of the two parameters increases the response more than what would be expected from the sum of their individual effects. This report further discusses the p-values and statistical significance of the calculated coefficients. A p-value describes the probability of obtaining the observed result, assuming that the null hypothesis is true [33]. In other words, the p-value represents the probability that the calculated relationship is a random coincidence and not in fact a true relationship. In this study, a p-value below 0.05 was chosen as the threshold for statistical significance.

The full interaction model was reduced iteratively in MODDE to retain predictive capability while removing weak contributors. This means that some response models had parameters or interaction terms removed because they did not make any contribution to the model.

5

Results

This chapter presents all results, from the manufacturing of cutting edges to the regression analysis of the test pieces. In the beginning, the manufactured cutting edges will be presented. Before that, this chapter will list all the results separately, and finally, the regression analysis from MODDE will be displayed, showing how each parameter affects surface integrity based on the gathered data.

5.1 Validation of test piece geometry

Figure 5.1 is a cross-section of one of the test pieces. There are no clear signs of strain in any direction other than the cutting direction, indicating that the test piece geometry is sufficient to analyze surface integrity. The only visible deformation can be seen at the top corners in the cross-section, just beneath the surface, where the thickness is slightly larger.

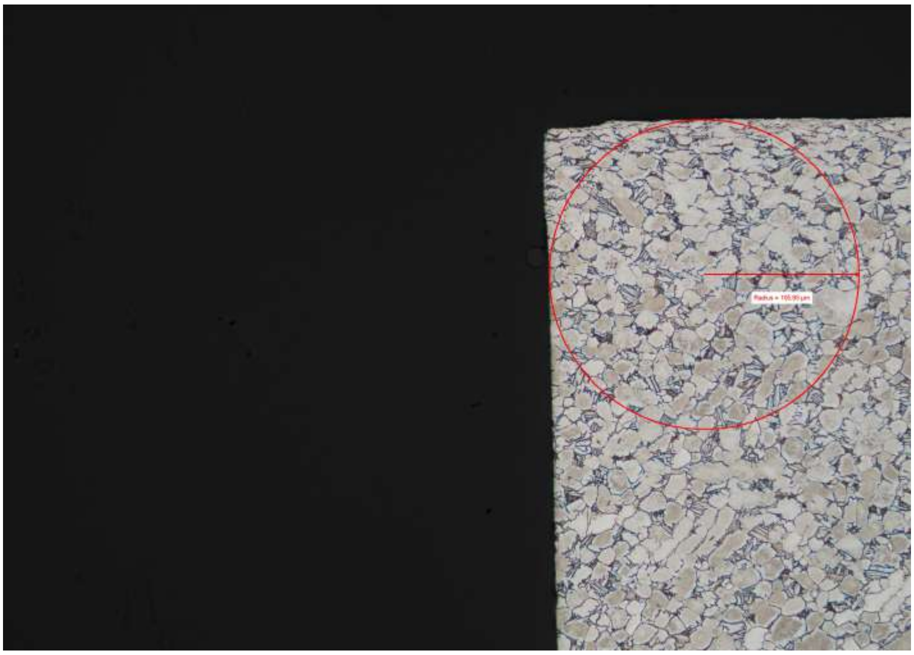

Figure 5.1: Photograph of the top left corner of the cross-section used for the validation of test piece geometry. Captured with the 5X objective.

5.2 Cutting edges used in experiments

Seven passages were done during the WEDM process, and the resulting surface of the cutting edges can be seen in Figure 5.3. Unfortunately, but as expected, the process was unable to produce cutting edges exactly according to the drawings. All radii were larger than intended, and S did not reach as large or small values as designed. Table 5.1 lists the geometry of the manufactured cutting edges. Figure 5.2 shows the plot of a measured radius from the MATLAB program that characterizes the micro-geometry.

Table 5.1: Micro-geometry of the manufactured cutting edge used in experiments. Radius = R.

Cutting edge	Intended R [µm]	Actual R [µm]	Intended S	Actual S	R^2
1	5	7.35	0.25	0.99	0.9951
2	35	43.70	0.25	0.30	0.9997
3	5	8.50	4	2.48	0.9983
4	35	44.40	4	3.35	0.99961
5	20	20.00	1	1.09	0.99974

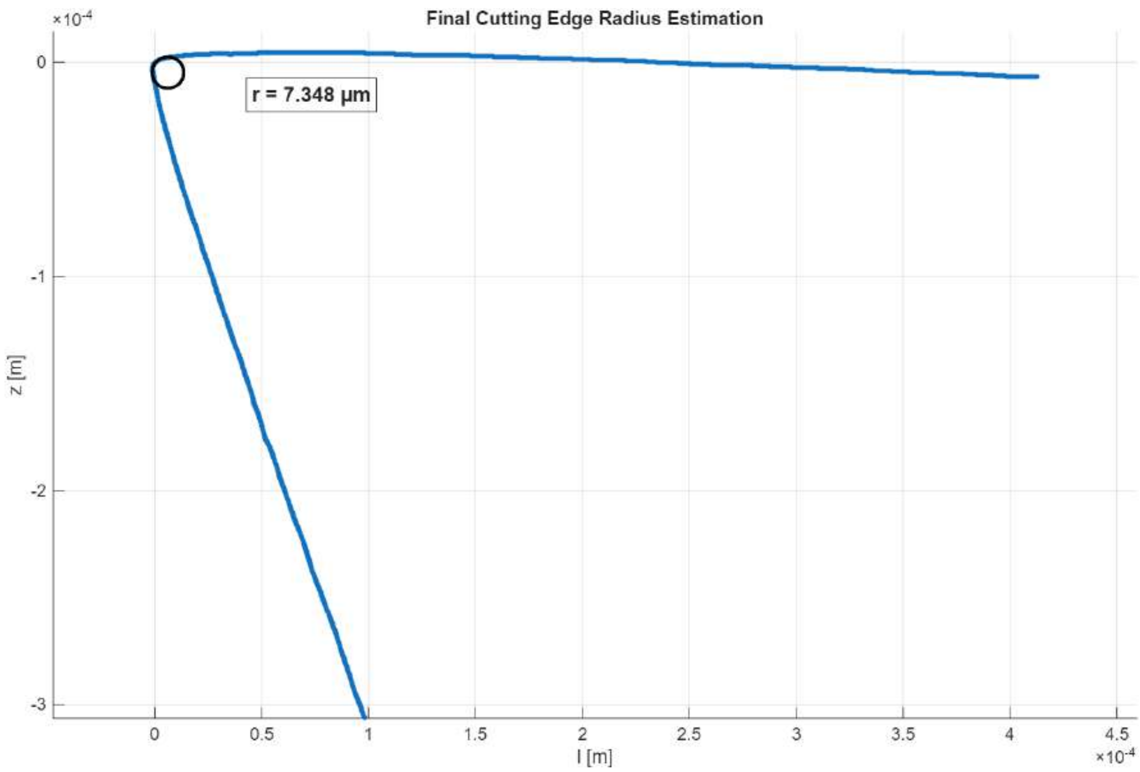

Figure 5.2: Plot of measured radius of Cutting Edge 1 in MATLAB.

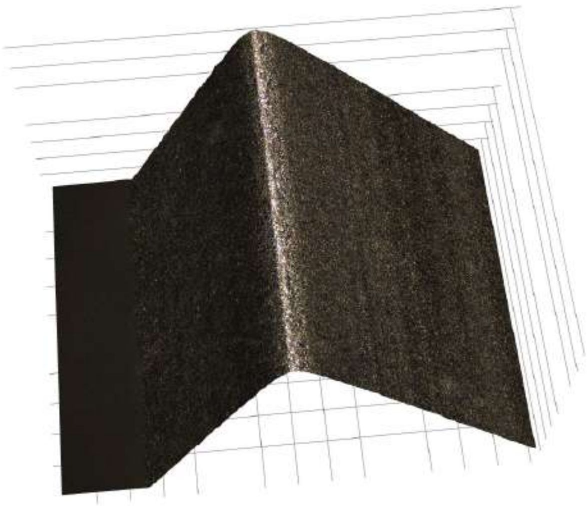

Figure 5.3: 3D measurement from a section of cutting edge 5 after WEDM. Captured with the 20X objective.

Since the micro-geometry of the cutting edges now differed from the values put into MODDE, the DOE needed to be updated. An updated version of the experiment plan can be found in Appendix C.

5.3 Process forces

Below are all the measured process forces that occurred during the different experiments. They are grouped in tables based on the cutting parameters that were used in order to better visualize the effect of micro-geometry.

5.3.1 Forces measured during main experiments

In all tables, there is one cutting edge that stands out, Cutting edge 2, with Radius = 43.7 µm and S = 0.30. It always generated the largest process forces. The cutting edges with smaller radii always generated larger process forces, except for the experiments in Table 5.4, where Experiment 9 with a small radius generated larger forces than Experiment 12 that used a large radius. Apart from that, there is no clear pattern among the other parameters that are visible without a regression analysis.

Table 5.2: Comparison between cutting edges 1-4 with $a_f = 0.05$ and $v_c = 2.50$

Exp. no.	Radius [µm]	S	a_f[mm]	v_c[m/min]	F_c[N]	F_f[N]
1	7.35	0.99	0.05	2.50	−475.53	313.19
2	43.70	0.30	0.05	2.50	−825.50	1776.55
3	8.50	2.48	0.05	2.50	−454.92	299.25
4	44.40	3.35	0.05	2.50	−530.01	495.83

Table 5.3: Comparison between cutting edges 1-4 with $a_f = 0.05$ and $v_c = 10.00$

Exp. no.	Radius [µm]	S	a_f[mm]	v_c[m/min]	F_c[N]	F_f[N]
5	7.35	0.99	0.05	10.00	−346.64	290.48
6	43.70	0.30	0.05	10.00	−872.62	1724.14
7	8.50	2.48	0.05	10.00	−405.06	261.17
8	44.40	3.35	0.05	10.00	−489.94	542.08

Table 5.4: Comparison between cutting edges 1-4 with $a_f = 0.10$ and $v_c = 2.50$

Exp. no.	Radius [µm]	S	a_f[mm]	v_c[m/min]	F_c[N]	F_f[N]
9	7.35	0.99	0.10	2.50	−803.19	352.12
10	43.70	0.30	0.10	2.50	−1103.95	1611.42
11	8.50	2.48	0.10	2.50	−694.12	281.29
12	44.40	3.35	0.10	2.50	−759.18	341.28

Table 5.5: Comparison between cutting edges 1-4 with $a_f = 0.10$ and $v_c = 10.00$

Exp. no.	Radius [µm]	S	a_f[mm]	v_c[m/min]	F_c[N]	F_f[N]
13	7.35	0.99	0.10	10.00	−675.41	349.96
14	43.70	0.30	0.10	10.00	−835.18	1497.96
15	8.50	2.48	0.10	10.00	−576.77	252.45
16	44.40	3.35	0.10	10.00	−696.61	585.29

Table 5.6: Comparison between cutting edge 5 with $a_f = 0.075$ and $v_c = 6.25$. This represents the middle points in all variable ranges.

Exp. no.	Radius [µm]	S	a_f [mm]	v_c[m/min]	F_c[N]	F_f[N]
17	20.00	1.09	0.075	6.25	−568.20	461.82
18	20.00	1.09	0.075	6.25	−580.31	440.90
19	20.00	1.09	0.075	6.25	−508.92	404.50

Figures 5.4 and 5.5 visualize the experimental data from the main experiments. They show how the variables vary across different cutting edge profiles.

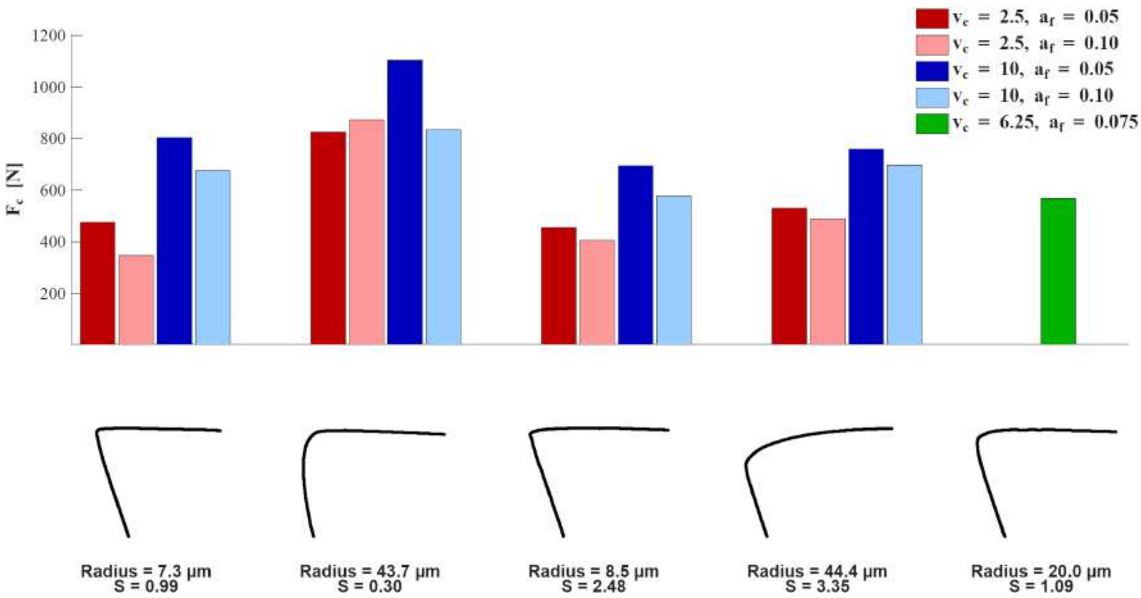

Figure 5.4: Plot that visualizes F_c from the main experiments.

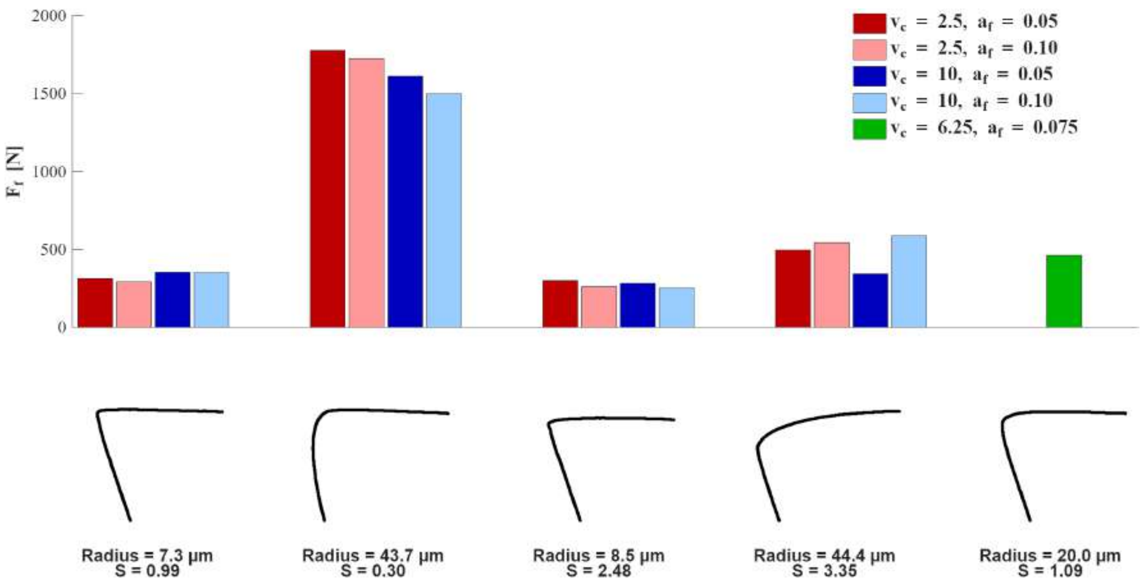

Figure 5.5: Plot that visualizes F_f from the main experiments.

5.3.2 Experiments without lubrication

Although dry machining trials were not conducted for every combination, the executed experiments demonstrate that the absence of lubrication alters the measured outcomes

Table 5.7: Comparison of all dry experiments.

Exp. no.	Radius [µm]	S	a_f [mm]	v_c[m/min]	F_c[N]	F_f[N]
20	20.00	1.09	0.075	6.25	−568.72	467.85
26	43.70	0.30	0.050	2.50	−1057.86	1412.60
27	8.50	2.48	0.050	2.50	−346.64	226.16
28	43.70	0.30	0.100	2.50	−959.64	1174.13
29	8.50	2.48	0.100	2.50	−693.60	279.29

5.3.3 Experiments with zero depth-of-cut

Even though the depth-of-cut was set to zero, small process forces were generated. However, Experiment 23 generated abnormally large forces and is a clear outlier.

Table 5.8: Comparison of experiments with zero depth at constant cutting speed.

Exp. no.	Radius [µm]	S	a_f[mm]	v_c[m/min]	F_c[N]	F_f[N]
21	20.00	1.09	0.00	2.50	−120.40	341.44
22	7.35	0.99	0.00	2.50	−11.65	38.47
23	43.70	0.30	0.00	2.50	−447.85	1272.28
24	8.50	2.48	0.00	2.50	−59.53	168.66
25	44.40	3.35	0.00	2.50	−139.16	367.43

5.4 Grain deformation

The sample preparation turned out well and provides clear images of the microstructural deformation. Figure 5.6 shows two different depths and degrees of deformation. The figure also gives clear evidence that different cutting edges used with the same process parameters perform differently.

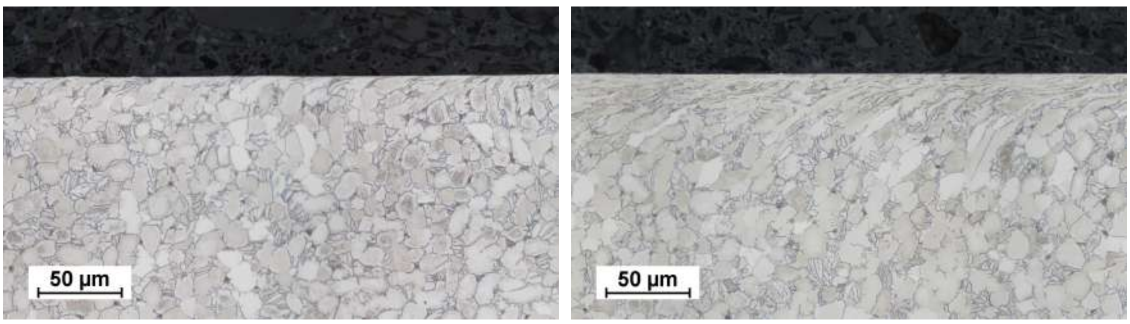

Figure 5.6: Comparison of grain boundary deformation between Experiment 13 (left) and Experiment 14 (right).

5.4.1 Grain deformation from main experiments

This section presents the microstructural deformation measured across the primary experiments. The results show that across all combinations of depth of cut and cutting speed, the cutting edge with Radius = 43.7 µm and S = 0.30 consistently produced the most microstructural deformation, both the deepest total deformation and the thickest amorphous layers.

Table 5.9: Total deformation and thickness of amorphous layer for experiments with a_f = 0.05 mm and v_c = 2.50 m/min.

Exp. no.	Radius [µm]	S	Tot. def. [µm]	σ_{td}[µm]	Amorphous [µm]	σ_a[µm]
1	7.35	0.99	9.08	1.72	0.00	0.00
2	43.70	0.30	34.54	2.18	1.97	1.80
3	8.50	2.48	5.28	1.93	0.00	0.00
4	44.40	3.35	16.14	4.35	0.00	0.00

Table 5.10: Total deformation and thickness of amorphous layer for experiments with a_f = 0.05 mm and v_c = 10.00 m/min.

Exp. no.	Radius [µm]	S	Tot. def. [µm]	σ_{td}[µm]	Amorphous [µm]	σ_a[µm]
5	7.35	0.99	10.68	3.72	1.12	1.30
6	43.70	0.30	31.08	8.94	6.69	2.32
7	8.50	2.48	9.44	1.71	0.00	0.00
8	44.40	3.35	10.48	2.42	1.94	1.91

Table 5.11: Total deformation and thickness of amorphous layer for experiments with a_f = 0.10 mm and v_c = 2.50 m/min.

Exp. no.	Radius [µm]	S	Tot. def. [µm]	σ_{td}[µm]	Amorphous [µm]	σ_a[µm]
9	7.35	0.99	8.59	3.00	0.00	0.00
10	43.70	0.30	35.16	7.61	5.71	2.39
11	8.50	2.48	10.97	2.09	1.70	0.71
12	44.40	3.35	15.24	3.54	3.89	0.34

Table 5.12: Total deformation and thickness of amorphous layer for experiments with a_f = 0.10 mm and v_c = 10.00 m/min.

Exp. no.	Radius [µm]	S	Tot. def. [µm]	σ_{td}[µm]	Amorphous [µm]	σ_a[µm]
13	7.35	0.99	5.54	1.03	0.00	0.00
14	43.70	0.30	37.08	6.13	10.73	1.60
15	8.50	2.48	6.39	1.01	0.00	0.00
16	44.40	3.35	12.32	1.43	3.86	1.12

Table 5.13: Total deformation and thickness of amorphous layer for center-point experiments.

Exp. no.	Radius [µm]	S	Tot. def. [µm]	σ_{td}[µm]	Amorphous [µm]	σ_a[µm]
17	20.00	1.09	13.86	2.92	3.48	0.87
18	20.00	1.09	13.48	1.34	4.61	1.26
19	20.00	1.09	13.58	2.50	2.88	0.34

Figures 5.7 and 5.8 visualize the experimental data from the main experiments. They show how the variables vary across different cutting edge profiles.

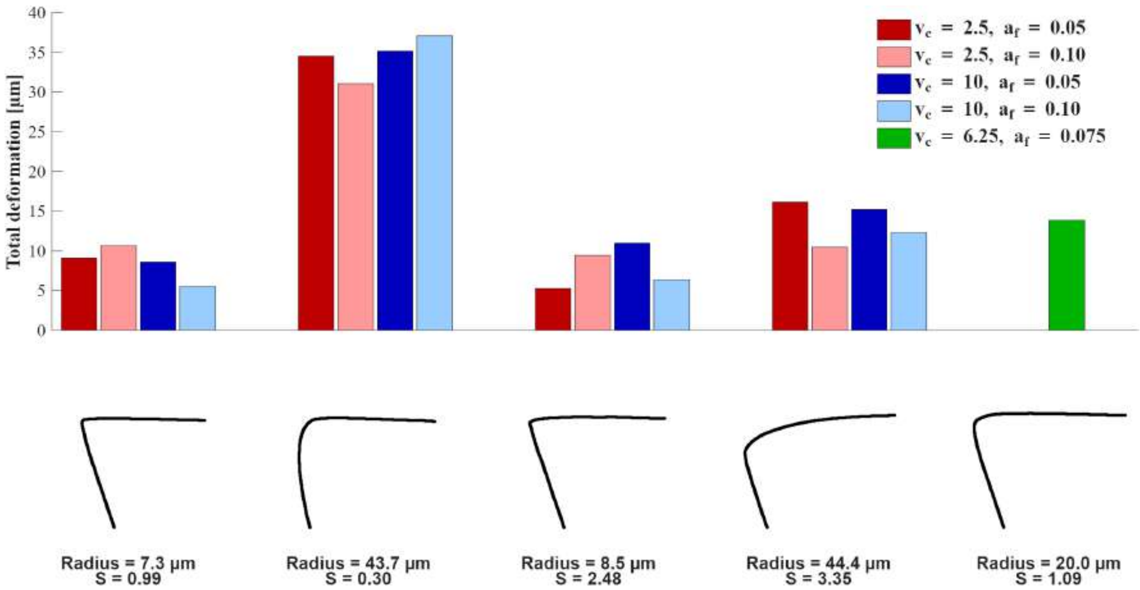

Figure 5.7: Plot that visualizes total deformation in the main experiments.

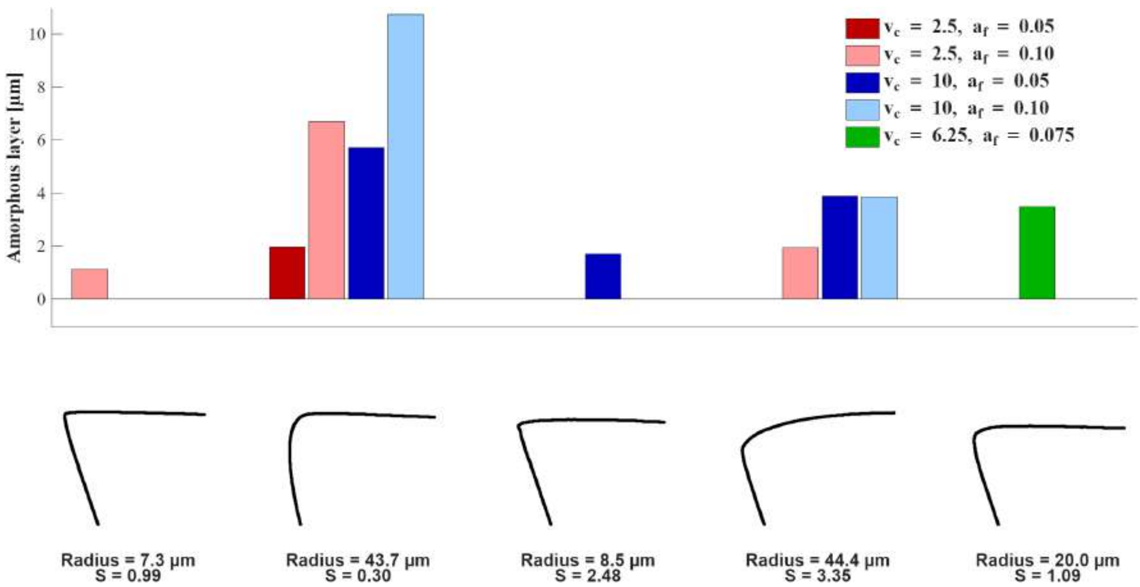

Figure 5.8: Plot that visualizes amorphous layer thickness in the main experiments.

5.4.2 Experiments with zero depth of cut

This section presents the microstructural deformation resulting from experiments where the nominal depth of cut was set to zero. Despite the absence of a programmed cutting depth, physical engagement between the tool and the workpiece still occurred, as can be seen by the force measurements.

Table 5.14: Measured amorphous layer from experiments with zero depth-of-cut.

Exp. no.	Radius [µm]	S	a_f[mm]	v_c[m/min]	Amorphous [µm]	σ_a[µm]
21	20.00	1.09	0.00	2.50	2.00	1.21
22	7.35	0.99	0.00	2.50	0.51	0.79
23	43.70	0.30	0.00	2.50	0.74	1.15
24	8.50	2.48	0.00	2.50	0.00	0.00
25	44.40	3.35	0.00	2.50	3.11	1.65

Table 5.15: Total deformation for experiments with zero depth-of-cut.

Exp. no.	Radius [µm]	S	a_f[mm]	v_c[m/min]	Tot. def. [µm]	σ_{td}[µm]
21	20.00	1.09	0.00	2.50	10.45	1.81
22	7.35	0.99	0.00	2.50	13.18	3.48
23	43.70	0.30	0.00	2.50	10.84	1.79
24	8.50	2.48	0.00	2.50	7.41	1.28
25	44.40	3.35	0.00	2.50	15.23	2.23

5.4.3 Experiments with no lubrication

As seen in the tables below, the tool with Radius = 43.7 µm and $S = 0.30$ produced a deep level of total deformation and thick amorphous layers up to 12.93 µm when operated without lubrication. The tool with Radius = 8.5 µm and $S = 2.48$ shows less plastic deformation when running without lubrication.

Table 5.16: Measured amorphous layer from experiments with no lubrication.

Exp. no.	Radius [µm]	S	a_f[mm]	v_c[m/min]	Amorphous [µm]	σ_a[µm]
20	20.00	1.09	0.08	6.25	3.04	0.98
26	43.70	0.30	0.05	2.50	11.23	3.45
27	8.50	2.48	0.05	2.50	0.00	0.00
28	43.70	0.30	0.10	2.50	12.93	1.00
29	8.50	2.48	0.10	2.50	0.00	0.00

Table 5.17: Total deformation depth for experiments with no lubrication.

Exp. no.	Radius [µm]	S	a_f[mm]	v_c[m/min]	Tot. def. [µm]	σ_{td}[µm]
20	20.00	1.09	0.08	6.25	12.45	2.01
26	43.70	0.30	0.05	2.50	40.06	6.74
27	8.50	2.48	0.05	2.50	8.01	1.31
28	43.70	0.30	0.10	2.50	43.97	9.28
29	8.50	2.48	0.10	2.50	10.18	1.58

5.5 Measured adhered material and surface tearing

The measured appearance of both these surface integrity phenomena was scattered, with high standard deviations and sometimes negative confidence intervals. The confidence intervals of the mean values for all experiments are found in Appendix C.

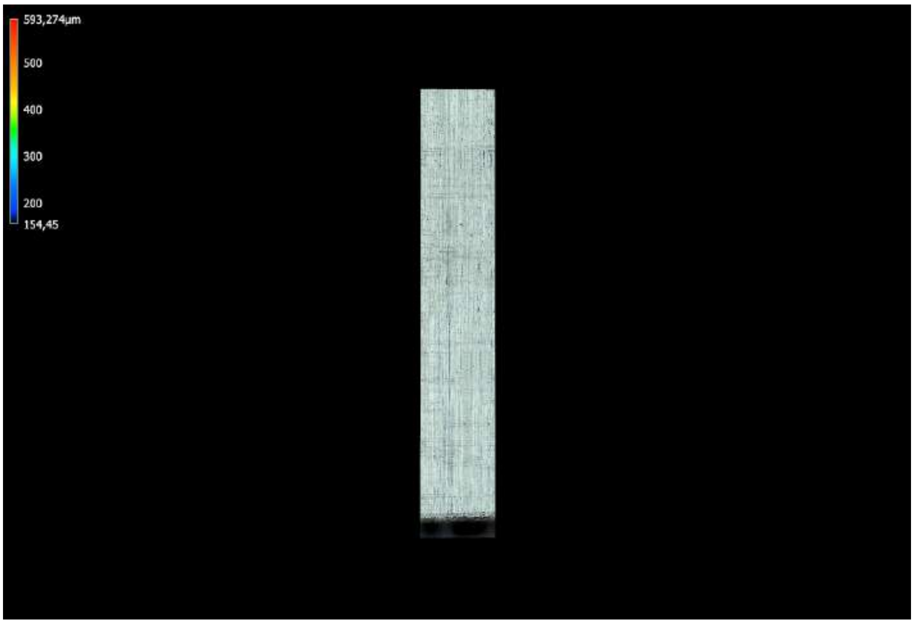

Figure 5.9: Multiple images stitched together to show an overview of the whole sample surface. Captured with the 5X objective.

5.5.1 Adhered material and surface tearing on main experiments

Table 5.18: Measured quantity of adhered material and surface tearing with $a_f = 0.05$ mm and $v_c = 2.50$ m/min.

Exp. no.	Radius [µm]	S	Mean surface tear	σ_{st}	Mean adhered	σ_{ad}
1	7.35	0.99	13.00	8.70	31.80	15.50
2	43.70	0.30	4.80	6.40	12.70	9.10
3	8.50	2.48	8.00	4.30	16.30	8.40
4	44.40	3.35	7.20	3.00	19.00	6.40

Table 5.19: Measured quantity of adhered material and surface tearing with $a_f = 0.05$ mm and $v_c = 10.00$ m/min.

Exp. no.	Radius [µm]	S	Mean surface tear	σ_{st}	Mean adhered	σ_{ad}
5	7.35	0.99	3.40	2.30	12.00	18.40
6	43.70	0.30	5.30	5.00	13.80	10.60
7	8.50	2.48	2.50	1.40	5.50	2.40
8	44.40	3.35	7.50	5.70	10.50	4.80

Table 5.20: Measured quantity of adhered material and surface tearing with $a_f = 0.10$ mm and $v_c = 2.50$ m/min.

Exp. no.	Radius [µm]	S	Mean surface tear	σ_{st}	Mean adhered	σ_{ad}
9	7.35	0.99	18.00	14.20	40.50	10.30
10	43.70	0.30	9.70	4.00	13.70	6.10
11	8.50	2.48	11.20	5.90	22.30	12.10
12	44.40	3.35	8.00	3.20	9.50	3.80

Table 5.21: Measured quantity of adhered material and surface tearing with $a_f = 0.10$ mm and $v_c = 10.00$ m/min.

Exp. no.	Radius [µm]	S	Mean surface tear	σ_{st}	Mean adhered	σ_{ad}
13	7.35	0.99	3.30	3.10	11.70	7.10
14	43.70	0.30	5.20	3.10	10.00	5.10
15	8.50	2.48	8.50	3.10	23.80	11.60
16	44.40	3.35	11.70	7.60	24.30	20.40

Table 5.22: Measured quantity of adhered material and surface tearing with $a_f =$ 0.075 mm and $v_c = 6.250$ m/min.

Exp. no.	Radius [µm]	S	Mean surface tear	σ_{st}	Mean adhered	σ_{ad}
17	20.00	1.09	4.20	3.90	14.80	9.30
18	20.00	1.09	5.00	0.00	17.00	0.00
19	20.00	1.09	2.00	1.80	7.50	6.70

Figures 5.10 and 5.11 visualize the experimental data from the main experiments. They show how the variables vary across different cutting edge profiles.

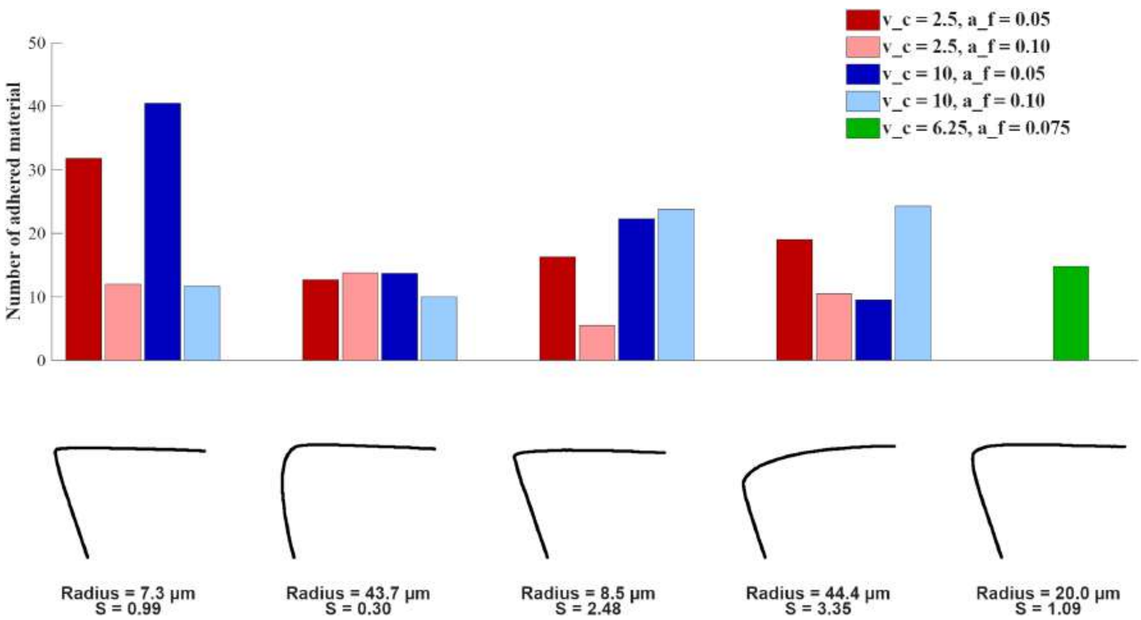

Figure 5.10: Plot that visualizes adhered material in the main experiments.

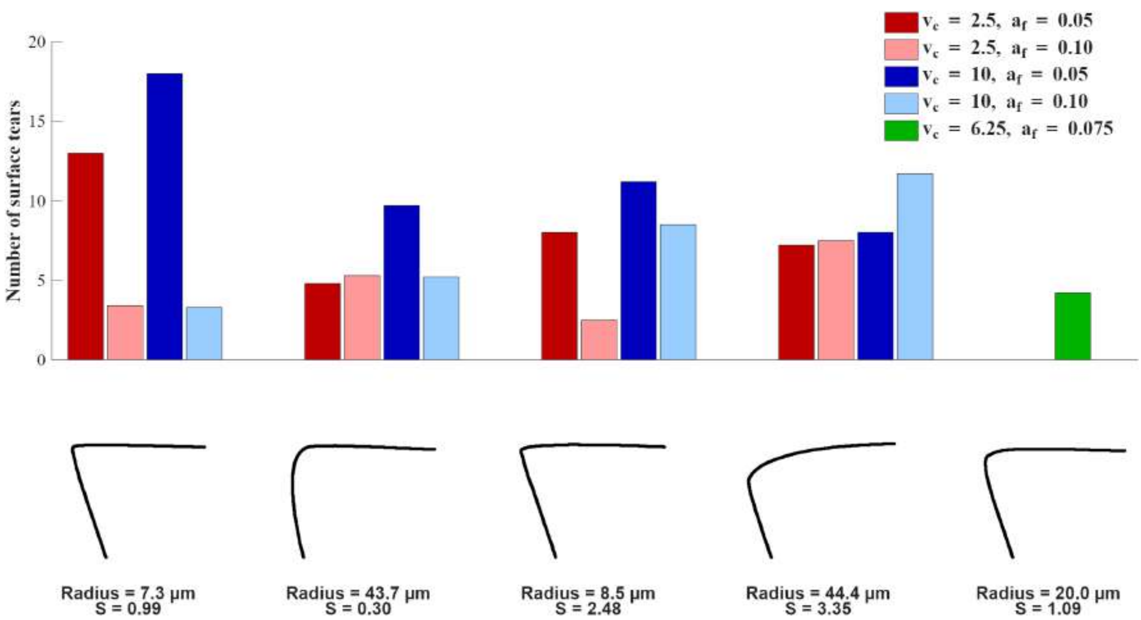

Figure 5.11: Plot that visualizes surface tearing in the main experiments.

5.5.2 Measured adhered material and surface tearing with no lubrication

This section outlines the topographical defects measured on the test pieces machined without lubrication. As in the main experiments, the amount of adhered material exhibited high standard deviation across the dry-machined surfaces.

Table 5.23: Surface tearing on samples with no lubrication.

Exp. no.	Radius [µm]	S	a_f[mm]	v_c[m/min]	Mean surface tear	σ_{st}
20	20.00	1.09	0.08	6.25	3.50	2.90
26	43.70	0.30	0.05	2.50	5.00	5.50
27	8.50	2.48	0.05	2.50	18.20	5.30
28	43.70	0.30	0.10	2.50	2.80	4.10
29	8.50	2.48	0.10	2.50	21.40	6.40

Table 5.24: Adhered material on samples with no lubrication.

Exp. no.	Radius [µm]	S	a_f[mm]	v_c[m/min]	Mean adhered	σ_{ad}
20	20.00	1.09	0.08	6.25	8.50	3.60
26	43.70	0.30	0.05	2.50	12.00	13.70
27	8.50	2.48	0.05	2.50	19.50	11.40
28	43.70	0.30	0.10	2.50	4.00	1.90
29	8.50	2.48	0.10	2.50	12.20	5.00

5.5.3 Measured adhered material and surface tearing with zero depth of cut

The results from the analysis on how zero depth of cut affects adhered material and surface tearing can be seen below. The data show that surface tearing peaked in Experiment 24, whereas adhered material was the highest in Experiment 23.

Table 5.25: Surface tearing in experiments with no depth-of-cut.

Exp. no.	Radius [µm]	S	a_f[mm]	v_c[m/min]	Mean surface tear	σ_{st}
21	20.00	1.09	0.00	2.50	8.00	7.00
22	7.35	0.99	0.00	2.50	10.70	4.70
23	43.70	0.30	0.00	2.50	13.00	5.40
24	8.50	2.48	0.00	2.50	24.80	9.50
25	44.40	3.35	0.00	2.50	9.70	3.70

Table 5.26: Adhered material on experiments with no depth-of-cut.

Exp. no.	Radius [µm]	S	a_f[mm]	v_c[m/min]	Mean adhered	σ_{ad}
21	20.00	1.09	0.00	2.50	9.30	6.10
22	7.35	0.99	0.00	2.50	16.70	9.20
23	43.70	0.30	0.00	2.50	19.00	15.20
24	8.50	2.48	0.00	2.50	12.80	5.30
25	44.40	3.35	0.00	2.50	14.20	13.50

5.5.4 Waviness

While the primary focus of this analysis was to quantify adhered material and surface tearing, the optical surface evaluation also revealed waviness in multiple tests. Measurements in Figure 5.12 revealed a maximum peak-to-valley waviness height of 18.69 µm and a spatial wavelength of approximately 3806 µm. To better illustrate the waviness, it has been magnified in Figure 5.13.

Figure 5.12: Experiment 14, showing 18.69 [µm] of waviness and a waviness length of 3806,09 [µm]

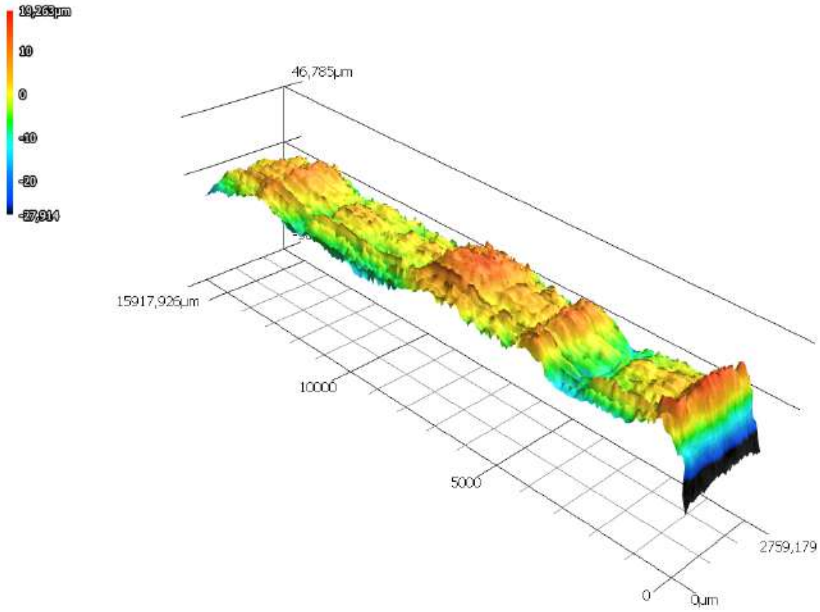

Figure 5.13: Picture showing a fully scanned coupon from experiment 14 and the cyclic waviness over its surface. Scanned using Keyence VK-X3000, Height amplification 3500%.

5.6 Residual stresses

5.6.1 Residual stresses from main experiments

Tables 5.27 to 5.31 show the measured longitudinal and transversal residual stresses for the main experiments. Since negative values correspond to compressive residual stresses, compressive stresses were observed in most experiments. Across all investigated process parameter combinations, the tool with a radius of 43.7 μm and $S = 0.3$ repeatedly resulted in the largest compressive residual stresses in both directions. Furthermore, variation between repeated measurements can be observed from the center-point experiments in Table 5.31, where different residual stress values were measured despite identical parameters.

Table 5.27: Measured residual stresses with $a_f = 0.05$ mm and $v_c = 2.50$ m/min.

Exp. no.	Radius [µm]	S	$\sigma_{res,long}$[MPa]	$\sigma_{res,trans}$[MPa]
1	7.35	0.99	49.90	341.80
2	43.70	0.30	−791.10	−842.80
3	8.50	2.48	−47.90	−253.30
4	44.40	3.35	−357.90	−306.90

Table 5.28: Measured residual stresses with $a_f = 0.05$ mm and $v_c = 10.00$ m/min.

Exp. no.	Radius [µm]	S	$\sigma_{res,long}$[MPa]	$\sigma_{res,trans}$[MPa]
5	7.35	0.99	−311.30	−128.70
6	43.70	0.30	−837.60	−458.40
7	8.50	2.48	−255.30	−148.80
8	44.40	3.35	−279.20	−270.90

Table 5.29: Measured residual stresses with $a_f = 0.10$ mm and $v_c = 2.50$ m/min.

Exp. no.	Radius [µm]	S	$\sigma_{res,long}$[MPa]	$\sigma_{res,trans}$[MPa]
9	7.35	0.99	−376.40	43.00
10	43.70	0.30	−1176.20	−882.70
11	8.50	2.48	−228.50	−95.00
12	44.40	3.35	181.80	210.00

Table 5.30: Measured residual stresses with $a_f = 0.10$ mm and $v_c = 10.00$ m/min.

Exp. no.	Radius [µm]	S	$\sigma_{res,long}$[MPa]	$\sigma_{res,trans}$[MPa]
13	7.35	0.99	18.30	71.80
14	43.70	0.30	−461.60	−326.70
15	8.50	2.48	−104.50	51.40
16	44.40	3.35	−384.10	−319.50

Table 5.31: Measured residual stresses with $a_f = 0.075$ mm and $v_c = 6.250$ m/min.

Exp. no.	Radius [µm]	S	$\sigma_{res,long}$[MPa]	$\sigma_{res,trans}$[MPa]
17	20.00	1.09	−162.10	−115.20
18	20.00	1.09	35.30	−96.80
19	20.00	1.09	−127.40	−499.10

Figures 5.15 and 5.14 visualize the experimental data from the main experiments. They show how the variables vary across different cutting edge profiles.

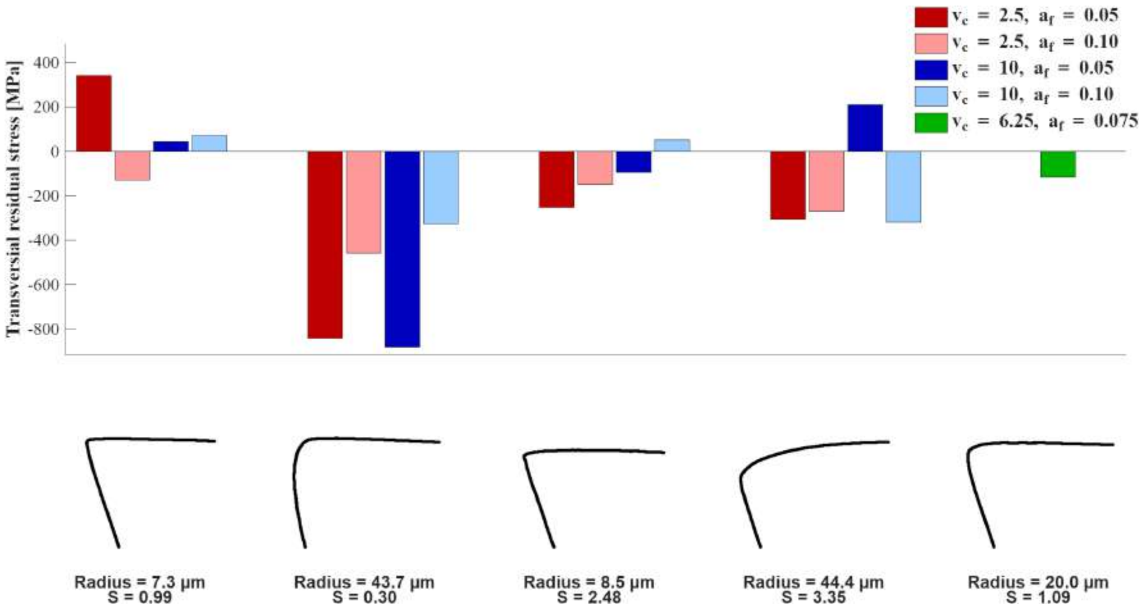

Figure 5.14: Plot that visualizes transversal residual stresses from the main experiments. Negative values are compressive stress.

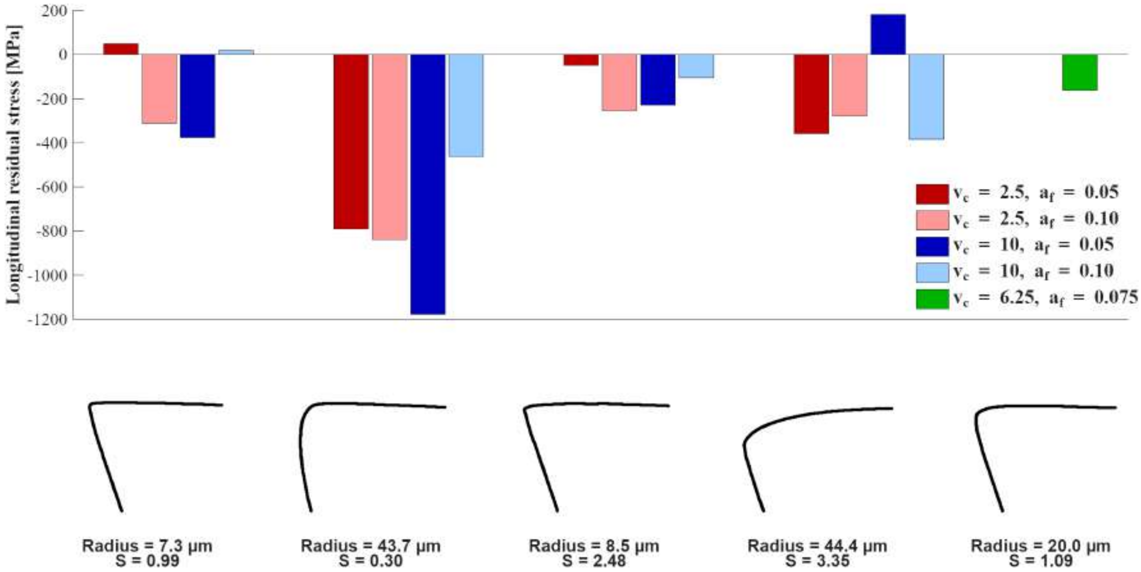

Figure 5.15: Plot that visualizes longitudinal residual stresses in the main experiments. Negative values are compressive stress.

5.6.2 Residual stresses with no lubrication

A comparison between the lubricated and dry experiments indicates some differences in the measured residual stresses. For the replicated experiments with Radius = 43.7 µm and S = 0.30, larger compressive residual stresses were generally observed without lubrication, particularly in the transversal direction. For the replicated experiments with Radius = 8.5 µm and S = 2.48, the differences were less consistent, although larger compressive stresses were observed in the longitudinal direction without lubrication.

Table 5.32: Measured residual stresses for experiments with no lubrication.

Exp. no.	Radius [µm]	S	a_f[mm]	v_c[m/min]	$\sigma_{res,long}$[MPa]	$\sigma_{res,trans}$[MPa]
20	20.00	1.09	0.08	6.25	−567.40	−241.40
26	43.70	0.30	0.05	2.50	−897.00	−1211.10
27	8.50	2.48	0.05	2.50	−249.30	−335.30
28	43.70	0.30	0.10	2.50	−989.10	−672.50
29	8.50	2.48	0.10	2.50	−467.10	−198.10

5.6.3 Residual stresses with zero depth-of-cut

A comparison between the experiments with zero depth-of-cut and their corresponding main experiments indicates differences in the measured residual stresses. For the tool with Radius = 43.7 μm and $S = 0.30$, larger compressive residual stresses were observed in both directions when the depth-of-cut was reduced to zero. A similar increase in compressive residual stress was observed in the transversal direction for the tool with Radius = 44.4 μm and $S = 3.35$. For the remaining replicated geometries, the observed changes were smaller or differed between directions.

Table 5.33: Experimental parameters and measured residual stresses for experiments with zero depth-of-cut

Exp. no.	Radius [µm]	S	a_f[mm]	v_c[m/min]	$\sigma_{res,long}$[MPa]	$\sigma_{res,trans}$[MPa]
22	7.35	0.99	0.00	2.50	−186.20	−91.70
23	43.70	0.30	0.00	2.50	−1209.30	−1305.60
24	8.50	2.48	0.00	2.50	−210.00	−739.90
25	44.40	3.35	0.00	2.50	−278.90	−719.40

5.7 Regression models

Below are the regression models describing each response variable from the main experiments. The equations represent the relationships between the process parameters and the response variables within the investigated design space and are therefore only valid within this range. Most models showed good fit and reproducibility, but model quality varied between responses. The calculated validation metrics used to assess model performance are presented in Appendix C.

5.7.1 Total deformation and amorphous layer thickness

Equations 5.1 and 5.2 describe the mathematical models relating the experimental parameters to total deformation and amorphous layer thickness. According to

Equation 5.1, total deformation increases with increasing radius and decreases with increasing S. Furthermore, the negative interaction term between radius and S indicates that their combined effect reduces total deformation relative to what would be expected from their individual effects alone.

$$\begin{aligned}\text{Total deformation} &= 13.88 + 6.38\mathit{Radius} - 4.93S \\ &\quad - 4.53(\mathit{Radius} \times S)\end{aligned} \tag{5.1}$$

$$\begin{aligned}\text{Amorphous layer} &= 2.19 + 1.48\mathit{Radius} - 1.29S + 0.68a_f + 0.62v_c \\ &\quad - 0.59(\mathit{Radius} \times S) + 0.48(\mathit{Radius} \times a_f) \\ &\quad + 0.68(\mathit{Radius} \times v_c) - 1.13(S \times a_f)\end{aligned} \tag{5.2}$$

Something that differs between the models for total deformation and amorphous layer is that only the model for amorphous layers is described by the effect of a_f and v_c, meaning that the described relationship remained no matter what process parameters were used in the experiments. An illustration of this can be seen in the figures 5.16-5.19, where surface plots have been made to visualize the regression models. The surfaces illustrating the model in Equation 5.1 remain the same even though a_f and v_c change.

Table 5.34: Regression coefficients and statistical evaluation for total deformation and amorphous layer thickness. Data from MODDE. Significant coefficients at a 95% confidence level are marked with *.

Variable	β_i	Std. Err.	P-value	Conf. Int. (±)
Total deformation				
Constant	13.88	0.671	< 0.001*	1.43
Radius	6.38	0.538	< 0.001*	1.15
S	-4.93	1.547	0.006*	3.30
Radius × S	-4.53	1.024	< 0.001*	2.18
Amorphous layer				
Constant	2.19	0.361	< 0.001*	0.80
Radius	1.48	0.289	< 0.001*	0.64
S	-1.29	0.832	0.151	1.85
a_f	0.68	0.329	0.064	0.73
v_c	0.62	0.315	0.079	0.70
Radius × S	-0.59	0.551	0.308	1.23
Radius × a_f	0.48	0.254	0.087	0.57
Radius × v_c	0.68	0.248	0.021*	0.55
S × a_f	-1.13	0.452	0.031*	1.01

All coefficients are statistically significant in the model for total deformation. Note that the coefficients for S and a_f are not significant alone, but their combined interaction term is statistically significant, showing a negative impact.

To visualize the interactions modeled by the regression equations, Figures 5.16 to 5.19 show how the micro-geometry of the cutting edge governs microstructural alterations under different machining conditions. Comparing Figures 5.16 and 5.17 reveals that increasing process parameters acts as a multiplier, shifting the majority of the damage plane upward and increasing the amorphous layer.

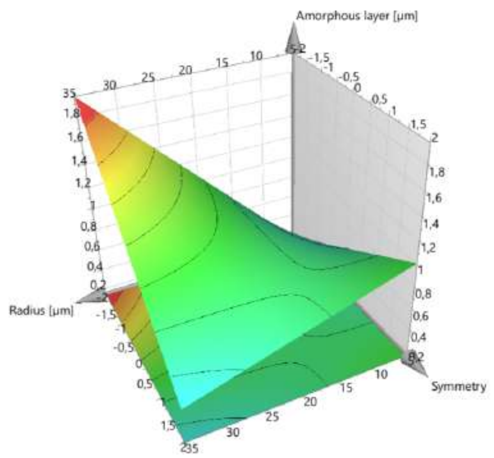

Figure 5.16: 3D surface plot of amorphous layer thickness as a function of radius and symmetry (depth of cut = 0.05 mm, v_c = 2.5 m/min).

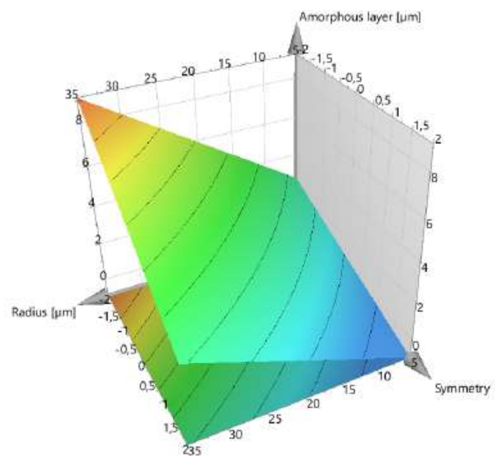

Figure 5.17: 3D surface plot of amorphous layer thickness as a function of radius and symmetry (depth of cut = 0.1 mm, v_c = 10 m/min).

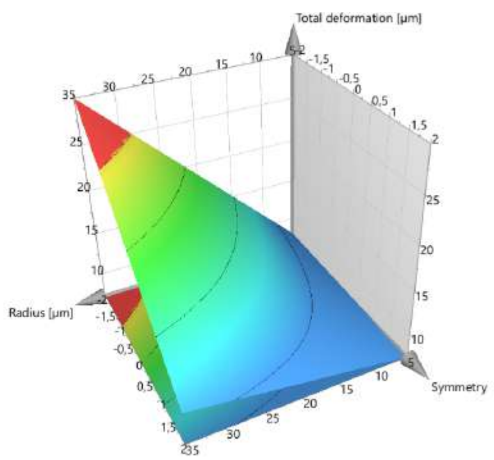

Figure 5.18: 3D surface plot of total deformation as a function of radius and symmetry (depth of cut = 0.05 mm, v_c = 2.5 m/min).

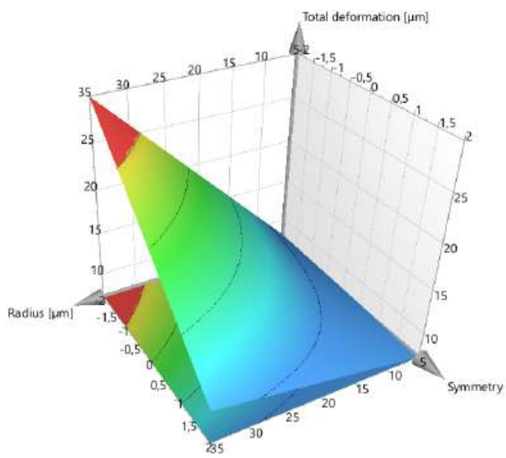

Figure 5.19: 3D surface plot of total deformation as a function of radius and symmetry (depth of cut = 0.1 mm, v_c = 10 m/min).

5.7.2 Surface tearing and adhered material

Equations 5.3 and 5.4 describe the mathematical models relating the experimental parameters to surface tearing and adhered material. According to Equation 5.3, surface tearing decreases with increasing a_f and increases with increasing v_c. Positive interaction terms between Radius and a_f, and between S and a_f, are also present in the model. Equation 5.4 shows that adhered material decreases with increasing Radius and a_f, while a positive interaction term between Radius and a_f is included in the model.

$$\begin{aligned} \text{Surface tearing} = 7.18 - 0.13 Radius + 1.05 S - 3.08 a_f + 1.49 v_c \\ + 1.93 (Radius \times a_f) + 1.71 (S \times a_f) \end{aligned} \tag{5.3}$$

$$\begin{aligned} \text{Adhered material} = 17.48 - 2.42 Radius - 4.69 a_f \\ + 3.27 (Radius \times a_f) \end{aligned} \tag{5.4}$$

Table 5.35: Regression coefficients and statistical evaluation for surface tearing and adhered material. Data from MODDE. Significant coefficients at a 95% confidence level are marked with *.

Variable	β_i	Std. Err.	P-value	Conf. Int. (±)
Surface tearing				
Constant	7.18	0.726	$< 0.001^*$	1.58
Radius	-0.13	0.612	0.831	1.33
S	1.05	1.095	0.355	2.39
a_f	-3.08	0.800	0.002^*	1.74
v_c	1.49	0.727	0.062	1.58
Radius × a_f	1.93	0.619	0.009^*	1.35
S × a_f	1.71	1.099	0.147	2.39
Adhered material				
Constant	17.48	1.748	$< 0.001^*$	3.73
Radius	-2.42	1.501	0.128	3.20
a_f	-4.69	1.922	0.027^*	4.10
Radius × a_f	3.27	1.514	0.048^*	3.23

For surface tearing, only a_f and Radius$\times a_f$ were significant apart from the constant term, and the same can be said about the model for the adhered material.

5.7.3 Process forces F_c and F_f

Equations 5.5 and 5.6 describe the mathematical models relating the experimental parameters to the process forces F_c and F_f. According to Equation 5.5, F_c increases with Radius and v_c, while it decreases with increasing S and a_f. Positive interaction terms between Radius and S, Radius and v_c, and between a_f and v_c are included in the model. Equation 5.6 shows that F_f increases with increasing Radius and decreases with increasing S, a_f, and v_c. Interaction terms between Radius and S, S and a_f, and S and v_c are also present in the model.

$$\begin{aligned} F_c = &-619.90 - 85.66 Radius + 80.75 S + 46.76 a_f - 117.17 v_c \\ &+ 55.48(Radius \times S) + 20.46(Radius \times v_c) \\ &+ 25.29(a_f \times v_c) \end{aligned} \tag{5.5}$$

$$\begin{aligned} F_f = &\, 558.19 + 330.55 Radius - 248.30 S - 15.03 a_f - 24.03 v_c \\ &- 249.58(Radius \times S) + 28.04(S \times a_f) \\ &+ 59.41(S \times v_c) \end{aligned} \tag{5.6}$$

Table 5.36: Regression coefficients and statistical evaluation for process forces. Data from MODDE. Significant coefficients at a 95% confidence level are marked with *.

Variable	β_i	Std. Err.	P-value	Conf. Int. (±)
F_c				
Constant	-619.90	20.276	< 0.001*	44.63
Radius	-85.66	16.263	< 0.001*	35.79
S	80.75	46.743	0.112	102.88
a_f	46.76	16.786	0.018*	36.95
v_c	-117.17	17.684	< 0.001*	38.92
Radius × S	55.48	30.940	0.100	68.10
Radius × v_c	20.46	13.935	0.170	30.67
a_f × v_c	25.29	16.786	0.160	36.95
F_f				
Constant	558.19	22.989	< 0.001*	50.60
Radius	330.55	18.439	< 0.001*	40.58
S	-248.30	52.997	< 0.001*	116.64
a_f	-15.03	19.567	0.459	43.07
v_c	-24.03	19.567	0.245	43.07
Radius × S	-249.58	35.079	< 0.001*	77.21
S × a_f	28.04	28.075	0.339	61.79
S × v_c	59.41	28.075	0.058	61.79

Among the statistically significant coefficients, the results show a strong relationship between micro-geometry and F_f, where both Radius and S were highly significant. Furthermore, the interaction term between Radius and S was also statistically significant, indicating that the influence of the micro-geometry parameters is represented both individually and in combination. For F_c, Radius and v_c were statistically significant as individual terms, whereas the interaction term between Radius and v_c was not statistically significant.

5.7.4 Residual stresses

Equations 5.7 and 5.8 describe the mathematical models relating the experimental parameters to the longitudinal and transversal residual stresses. Since negative values correspond to compressive residual stresses, the negative coefficients for Radius indicate increasing compressive stresses with increasing Radius in both directions. Radius was statistically significant in both models, whereas the remaining main effects were not statistically significant. In the transversal model, the interaction term between Radius and S was also statistically significant.

$$\begin{aligned}\text{Longitudinal } \sigma_{res} &= -237.72 - 162.21 Radius + 82.49 S + 29.17 a_f \\ &+ 169.49(Radius \times S) - 144.96(S \times a_f)\end{aligned} \tag{5.7}$$

$$\begin{aligned}\text{transversal } \sigma_{res} &= -128.28 - 180.22 Radius - 50.04 S + 37.09 a_f \\ &+ 197.10(Radius \times S) - 145.68(S \times a_f)\end{aligned} \tag{5.8}$$

Table 5.37: Regression coefficients and statistical evaluation for residual stresses. Data from MODDE. Significant coefficients at a 95% confidence level are marked with *.

Variable	β_i	Std. Err.	P-value	Conf. Int. (±)
Longitudinal residual stress				
Constant	-237.72	60.273	0.002*	130.21
Radius	-162.21	49.121	0.006*	106.12
S	82.49	136.785	0.557	295.51
Depth of cut	29.17	54.407	0.601	117.54
Radius × S	169.49	91.295	0.086	197.23
S × a_f	-144.96	77.951	0.086	168.40
Transversal residual stress				
Constant	-128.28	59.344	0.050*	128.21
Radius	-180.22	48.364	0.003*	104.48
S	-50.04	134.677	0.716	290.95
Depth of cut	37.09	53.569	0.501	115.73
Radius × S	197.10	89.888	0.047*	194.19
S × a_f	-145.68	76.750	0.080	165.81

5.8 Summary of results

To provide the reader with a more comprehensive overview of the experiments and the resulting characteristics, the key process parameters and variables are listed in Table 5.38.

Table 5.38: Summary of experimental parameters, cutting forces, deformation metrics, and residual stresses

Exp.	*Radius* [μm]	S	a_f [mm]	v_c [m/min]	F_c [N]	F_f [N]	Mean def. depth [μm]	Std. depth	Mean Amorph. layer [μm]	Std. Amorph.	Mean tear-offs	Std. tear-offs	Mean adhered	Std. adhered	Long. res. stress [MPa]	Cross. res. stress [MPa]
1	7.35	0.99	0.05	2.50	−475.53	313.19	9.08	1.72	0.00	0.00	13.00	8.70	31.80	15.50	49.90	341.80
2	43.70	0.30	0.05	2.50	−825.50	1776.55	34.54	2.18	1.97	1.80	4.80	6.40	12.70	9.10	−791.10	−842.80
3	8.50	2.48	0.05	2.50	−454.92	299.25	5.28	1.93	0.00	0.00	8.00	4.30	16.30	8.40	−47.90	−253.30
4	44.40	3.35	0.05	2.50	−530.01	495.83	16.14	4.35	0.00	0.00	7.20	3.00	19.00	6.40	−357.90	−306.90
5	7.35	0.99	0.05	10.00	−346.64	290.48	10.68	3.72	1.12	1.30	3.40	2.30	12.00	18.40	−311.30	−128.70
6	43.70	0.30	0.05	10.00	−872.62	1724.10	31.08	8.94	6.69	2.32	5.30	5.00	13.80	10.60	−837.60	−458.40
7	8.50	2.48	0.05	10.00	−405.06	261.17	9.44	1.71	0.00	0.00	2.50	1.40	5.50	2.40	−255.30	−148.80
8	44.40	3.35	0.05	10.00	−489.94	542.08	10.48	2.42	1.94	1.91	7.50	5.70	10.50	4.80	−279.20	−270.90
9	7.35	0.99	0.10	2.50	−803.11	352.22	8.59	3.00	0.00	0.00	18.00	14.20	40.50	10.30	−376.40	43.00
10	43.70	0.30	0.10	2.50	−1103.95	1611.42	35.16	7.61	5.71	2.39	9.70	4.00	13.70	6.10	−1176.20	−882.70
11	8.50	2.48	0.10	2.50	−694.12	281.29	10.97	2.09	1.70	0.71	11.20	5.90	22.30	12.10	−228.50	−95.00
12	44.40	3.35	0.10	2.50	−759.18	541.50	15.24	3.54	3.89	0.34	8.00	3.20	9.50	3.80	181.80	210.00
13	7.35	0.99	0.10	10.00	−675.41	349.96	5.54	1.03	0.00	0.00	3.30	3.10	11.70	7.10	18.30	71.80
14	43.70	0.30	0.10	10.00	−835.18	1497.96	37.08	6.13	10.73	1.60	5.20	3.10	10.00	5.10	−461.60	−326.70
15	8.50	2.48	0.10	10.00	−576.77	252.45	6.39	1.01	0.00	0.00	8.50	3.10	23.80	11.60	−104.50	51.40
16	44.40	3.35	0.10	10.00	−696.61	585.29	12.32	1.43	3.86	1.12	11.70	7.60	24.30	20.40	−384.10	−319.50
17	20.00	1.09	0.08	6.25	−568.20	461.82	13.86	2.92	3.48	0.87	4.20	3.90	14.80	9.30	−162.10	−115.20
18	20.00	1.09	0.08	6.25	−580.31	440.90	13.48	1.34	4.61	1.26	5.00	0.00	17.00	0.00	35.30	−96.80
19	20.00	1.09	0.08	6.25	−508.92	404.50	13.58	2.50	2.88	0.34	2.00	1.80	7.50	6.70	−127.40	−499.10
20	20.00	1.09	0.08	6.25	−568.72	467.85	12.45	2.01	3.04	0.98	3.50	2.90	8.50	3.60	−567.40	−241.40
26	43.70	0.30	0.05	2.50	−1057.86	1412.60	40.06	6.74	11.23	3.45	5.00	5.50	12.00	13.70	−897.00	−1211.10
27	8.50	2.48	0.05	2.50	−346.64	226.16	8.01	1.31	0.00	0.00	18.20	5.30	19.50	11.40	−249.30	−335.30
28	43.70	0.30	0.10	2.50	−959.64	1174.13	43.97	9.28	12.93	1.00	2.80	4.10	4.00	1.90	−989.10	−672.50
29	8.50	2.48	0.10	2.50	−693.60	279.29	10.18	1.58	0.00	0.00	21.40	6.40	12.20	5.00	−467.10	−198.10

6
Discussion

The discussion consists of several reviews of the results in previous chapters and how it connects to research. It emphasizes what has impacted the results and how it can be prevented in the future. Finally, it summarizes this study's contribution to this field of science.

6.1 Manufacturing method of cutting edges

All cutting edges were manufactured with WEDM, and based on the resulting edges, the process used needs to be altered. The machined surface was of a rather high quality, which can be seen in Figure 5.3. The geometry did not turn out as expected. The error appears to follow a specific pattern, where all edges except the one with center values of radius and symmetry deviated in size from the intended value. This suggests that the error might be linked to tools with significant asymmetry, as the cutting edge with $S = 1$ has the same radius as originally designed. A possible cause could be that the wire takes a shortcut when trying to move along these kinds of geometries. It is unlikely that this error has anything to do with the characterization method for micro-geometry since the same MATLAB program has been used to measure both the edges in CAD and the actual edges.

6.2 Review of results

In this section, discussions about the results from the experiments will take place. Comparisons with previous research and reasoning about the meaning of the results will be presented here.

6.2.1 Microstructural deformation

The regression analysis clearly showed that both edge radius and symmetry strongly dictate the level of amorphous layer and total deformation. As can be seen in Table 5.34, the regression model is best fitted by excluding a_f and v_c, which suggests that the identified relationship between cutting edge micro-geometry and surface integrity holds across all combinations of process parameters used in this study. Hu et al. [24] received similar results from their finite element simulation model. Interestingly, the interaction term Radius $\times$ S mathematically shows that the total deformation usually caused by a large tool radius can be reduced if the tool is designed with a trumpet-shaped profile ($S > 1$).

Amorphous layer thickness, on the other hand, depended on more parameters than just the micro-geometry, something that can be seen in Figures 5.16 and 5.17. Something worth mentioning when discussing the resulting amorphous layers is the standard deviation. The ratios between mean value and standard deviation for the amorphous layers are, in general, larger than those for total deformation. What this means is that the amorphous layer thickness varied more within test pieces than the total deformation.

Before the zero-depth pass was performed, a conventional cut was first made to prepare the test surface. Consequently, the measured deformation represents the combined effect of both operations rather than the effect of the zero-depth pass alone. Notably, the cutting edge with Radius = 7.35 µm and $S = 0.99$ received both deeper total deformation and amorphous layer thickness after the cut with zero depth. While any increase in deformation compared to similar experiments from the main test series may indicate that the additional pass contributed further plastic deformation, the present methodology does not allow the deformation generated exclusively by the zero-depth pass to be quantified.

The dry experiments suggest that the absence of lubrication may increase subsurface deformation for certain cutting edges, particularly those already prone to producing deep deformation. However, the same trend was not consistently observed across all tested geometries.

6.2.2 Process forces

The results from simulations by A. S. Ertürk [21] and the findings by Gertsenmeyer et al. [19] align with the trends observed in this study. Their simulations showed that cutting edges with $\kappa < 1$, a waterfall-shaped edge, generate larger process forces, which is the same relationship that is described in Table 5.36. It is important to remember when making these comparisons that S and κ are roughly the same, at least they always have the same sign. The coefficient in Table 5.36 shows that if you increase S by one step, F_c increases by 80.75 steps. The alignment of the findings suggests that it is possible that the trends seen in this study, at least regarding process forces, exist outside the design space of the experiments in this thesis. Furthermore, A. S. Ertürk [21] also simulated what happened when S_γ and S_α increased while maintaining the same κ, effectively decreasing the radius, but those results instead contradict the results in this study. Table 5.36 describes the relationship as if the radius is increased, both F_c and F_f increase.

The effect of cutting edge micro-geometry on the process forces has been identified. However, it does not stay the same regardless of the depth of cut and cutting speed. According to the regression model made by MODDE, these two process parameters also have an effect on the forces. Even though they did not always have significant p-values, the model was best fitted with them included.

The additional experiments revealed that the removal of lubrication did not result in a clear or consistent change in the process forces. For the center-point geometry, the measured forces under dry conditions were very similar to those obtained during the lubricated experiments, while the remaining dry experiments showed both increases and decreases depending on the cutting-edge geometry. In contrast, the experiments performed with zero depth-of-cut generated substantially lower forces than the main experiments, although measurable forces were still present. This suggests that a significant portion of the process forces originates from ploughing and rubbing between the cutting edge and the test-piece surface, even when no material is removed.

6.2.3 Insufficient method for characterizing adhered material and surface tearing

Already before the regression analysis was finished, it was possible to see that the amount of adhered material and surface tearing was inconsistent. The results were scattered, and the standard deviation was high. The calculations of the confidence limits further acknowledged this.

One limitation of this method is that adhered material can increase the average surface height. As a result, concave features with an actual depth below 0.2 µm may be incorrectly identified as deeper than the threshold, leading to false detections of surface tearing.

Furthermore, stitched images obtained with the 5X objective showed that adhered material and surface tearing were unevenly distributed, occurring in localized clusters (Figure 5.9). Since the analysis was based on only six high-magnification images, such regions could easily be missed. Consequently, a sample containing localized but potentially critical defects may still be classified as having an acceptable surface condition.

The regression analysis showed that the cutting-edge micro geometry alone did not have a statistically significant effect on either the amount of adhered material or the occurrence of surface tearing. However, significant effects from a_f were observed. This indicates that the influence may depend on the selected cutting conditions rather than cutting edge micro-geometry. Consequently, no clear direct relationship between micro-geometry and these surface defects could be established, although such a relationship cannot be ruled out. Furthermore, the close association observed between adhered material and surface tearing suggests that the two features may be linked through the same underlying mechanisms. It should also be noted that the characterization method may have contributed to this apparent relationship. As mentioned before, the threshold-based detection method may incorrectly classify normal surface features as surface tearing. Therefore, the observed correlation between adhered material and surface tearing should be interpreted with caution.

The dry experiments did not reveal a consistent effect of lubrication on adhered material and surface tearing. While some cutting edges exhibited noticeably higher levels of surface tearing under dry conditions, other geometries produced results comparable to those obtained during lubricated cutting. The influence of lubrication, therefore, appeared to depend on the selected cutting edges rather than acting as an independent factor. However, due to the limited number of dry experiments and the previously discussed uncertainties associated with the characterization method, these observations should be regarded as indications rather than trends.

6.2.4 Residual stresses

Looking at the residual stresses from the machining, there is an outlier among the cutting edges. The blunt waterfall edge, $R = 43.7$ µm, $S = 0.30$, especially when used at a deeper depth of cut and a lower speed, generated a significant longitudinal compressive stress of -1176.2 MPa. Because the symmetry factor is well below 1, the bulk of the tool's radius is shifted downward onto the flank face. Instead of guiding the titanium up the rake face to form a chip, it forces the tool to ride over the test piece. This can also be seen in the force data as the feed force, pushing the tool away from the workpiece, violently spiked to nearly 1800 N, exceeding the forces generated by the sharper or more symmetrical tools. The results gathered by Denkena and Biermann [3] support this, as the authors came to the conclusion that larger tool radii increase compressive residual stresses.

When looking at the regression model, it should be considered that both a decrease and an increase in residual stress could mean improved surface integrity. This depends on whether one is analyzing compression or tension of the material. For example, the model states that increasing the radius by one step decreases the longitudinal residual stresses by 162.21 steps. This is good with tension stresses in mind, since that means a decrease in residual stresses, but not favorable with compressive stresses in mind, since it means an increase in residual stresses. The regression model does not consider this and should be remembered while interpreting the results.

It should also be noted that the data is scattered and longitudinal stresses fluctuated between a tensile state of 35.3 MPa and a compressive state of -162.1 MPa. This variance does not invalidate the overarching micro-geometrical trends observed; however, it shows how stress generation is a highly sensitive phenomenon. An example is how variations in the surface topography can distort the diffraction of the XRD, altering the reading.

The dry experiments generally resulted in more compressive residual stresses than the corresponding lubricated experiments. This tendency was most evident for the cutting edge with a radius of 43.7 µm and $S = 0.30$, where both longitudinal and transversal stresses became noticeably more compressive when lubrication was removed. A similar tendency was observed for the centre-point experiment. Although the limited number of dry experiments prevents any definitive conclusions, and no regression analysis has been performed, the results suggest that lubrication may influence the residual stresses more than it influences process forces or subsurface deformation.

The residual stresses measured after the experiments with zero depth-of-cut differed from those measured in the corresponding main experiments. The largest differences were observed for the cutting edge with a radius of 43.7 µm and S = 0.30, which resulted in more compressive residual stresses in both directions. Increased compressive stresses were also observed for some of the other geometries, particularly in the transversal direction. These observations suggest that the additional cut with no depth influenced the residual stresses. However, since only the final residual stresses were measured on the same sample, the exact contribution of the cuts cannot be quantified.

6.3 Review of regression models

The quality of the fitted regression models varied between the different response variables, which can be seen in Table C.14. The models developed for the process forces and total deformation demonstrated a strong ability to describe the observed variation in the experimental data while also exhibiting good predictive capability. This indicates that the selected process parameters captured the dominant trends in these responses and that the resulting models were suitable for analyzing the effects of the investigated factors within the experimental design space.

The model for amorphous layer thickness also showed satisfactory performance, although its predictive capability was somewhat weaker than that of the force and deformation models. Nevertheless, the model was able to explain a substantial portion of the observed variation and provided a reasonable basis for interpreting the effects of the investigated factors.

In contrast, the models for surface tearing and adhered material exhibited lower performance. A larger proportion of the variation remained unexplained, and the predictive capability was limited, particularly for adhered material. This is consistent with the observations discussed previously, where both responses displayed considerable scatter and large variations between measurements. The uneven distribution of defects across the machined surface and the limitations of the characterization method likely contributed to the reduced model quality. Consequently, conclusions regarding these responses should be interpreted with greater caution than for those related to forces, deformation, and amorphous layer thickness.

The models developed for the longitudinal and transversal residual stresses showed intermediate performance compared to the other responses. Both models were able to capture a meaningful portion of the variation in the experimental data, indicating that the investigated process parameters influenced the residual stresses. However, the predictive capability was noticeably lower than that of the force, deformation, and amorphous layer models. This suggests that although the models were suitable for identifying general trends and evaluating factor effects within the experimental design space, a substantial part of the variation remained unexplained. Consequently, interpretations of the residual stress results should be made with a greater degree of caution than those of the strongest performing models.

It should also be noted that non-significant terms were retained in the final models. The model selection procedure in MODDE was based on achieving the best overall balance between descriptive ability, predictive performance, and model robustness rather than solely removing terms based on their individual statistical significance. However, when interpreting the physical relationships between process parameters and the responses, primary emphasis was placed on effects that were found to be statistically significant.

6.4 Review of experiment setup

One aim of the thesis was to develop a consequential, robust, and repeatable test method for these kinds of experiments that could be used for similar experiments in the future. Overall, the aim has been fulfilled, but there are a few minor adjustments that could improve the method, other than what has already been mentioned about the manufacturing of cutting edges.

If this test method is going to be used again, a standardized way of lubricating the tool and test piece needs to be implemented. Throughout this study, the lubricant has been added by applying oil to the test piece and tool before the test. This has neither controlled the amount of applied oil nor ensured that the whole tool and test piece are covered properly. The amount of lubrication can have an effect on process forces or surface integrity.

6.5 Possible impacts on the study

Several factors may have affected the results obtained. The following are possible things that should be considered when interpreting the results. While they do not invalidate the observed trends, they may reduce the strength of the results.

6.5.1 Manual measurement of total deformation and amorphous layer

All measurements of the microstructure were done manually by the same person, which means that there was room for human errors, a possible underlying reason for incorrect measurements. These possible errors could contribute to a wrong mean value being calculated, which then feeds the regression model with faulty values. Identifying the end of the total deformation or amorphous layer is not a simple task. However, since the same person measured all layers in a consistent manner, it removes errors between different operators.

6.5.2 Compliance

While analyzing some test pieces, it could be observed to exhibit waviness, as seen in figure 5.12 and 5.13. A possible reason for this is that compliance in either the workpiece, fixture, or machine tool may result in deflections during machining. These deflections can lead to periodic variations in the depth of cut, resulting in waviness on the surface. Another possible factor could be the cutting edge geometry. If the cutting forces vary along the tool path. As this may interact and amplify the system compliance, resulting in uneven material removal.

As mentioned earlier, the stitched image in Figure 5.9 revealed that adhered material and surface tearing were not uniformly distributed across the test pieces, but instead often appeared in concentrated clusters. This inhomogeneous distribution may be a consequence of compliance, which could also explain the relatively high standard deviation observed in the amorphous layer thickness.

6.5.3 Choice of micro-geometry characterization method

When drawing parallels to other research papers within the same scientific field, it is important to remember that different ways to characterize micro-geometry have been used. Therefore, the stated effects from other researchers would probably not have been the same if they used the method by Wyen et al. [10]. Although it would have had an effect, there is nothing that indicates that the results would differ so much that any derived effects on surface integrity changes sign from positive to negative, or vice versa. It is therefore still relevant to compare the trends discovered in this thesis to other research papers that have analyzed the effect of micro-geometry.

The method for characterizing micro-geometry in this study allows for consistent results. The impact of micro-geometry has not been affected by human error or measurement variations. However, what is not verified is the point uncertainty in the Alicona EdgeMaster, the program used to create the data points. Though it is probably very low, it is worth mentioning that point uncertainty affects the calculated geometry, which influences this whole study.

7
Conclusion

Several orthogonal cutting experiments have been made in order to identify the influence of cutting edge micro-geometry on surface integrity. Data have been gathered and analyzed through both already existing methods and methods developed in this thesis. An iterative method to characterize cutting edge micro-geometry.

This study has described the effect cutting edge micro-geometry has on surface integrity. However, all surface integrity variables could not be described from these experiments. The list below summarizes conclusions supported by statistical analysis concerning the influence of cutting edge micro-geometry on surface integrity, including parameters for which no significant effect was observed.

- Larger radius increases total deformation, amorphous layer thickness, cutting force, feed force, and residual stresses.
- $S > 1$ generates lower total deformation and feed force, while $S < 1$ gives the opposite results.
- This study did not reveal any influence of cutting edge micro-geometry on adhered material and surface tearing. The same can be said about the effect of S on amorphous layer thickness, cutting force, and residual stresses.

If similar experiments will take place at GKN Aerospace in the future, the method for characterizing adhered material and surface tearing needs to be considered. Furthermore, the manufacturing of cutting edges needs improvement, as the desired geometries could not be achieved.

7.1 Recommendations for future work

Further research could begin with exploring different and yet undefined areas of the cutting edge. One example could be the distance from the tool tip to the cutting depth, something that automatically changes when altering the radius and symmetry.

Another interesting question to answer is if the observed variations within each sample have anything to do with micro-geometry. Compliance probably is a major factor, but it should not be ruled out that some geometries create less stable cutting operations. One way to begin is to perform a regression analysis with the calculated standard deviations, as that would show if there is any statistical relationship between micro-geometry and deviations within samples.

Declaration of AI usage

AI-assisted tools, including Grammarly and ChatGPT, were used as support at some occasions in this thesis. These tools were primarily employed for language support, such as improving grammar, sentence structure, clarity, and conciseness. In addition, they were used to assist in the development and refinement of the programming code utilized in this work.

Bibliography

[1] GKN Aerospace, *Produkter och tjänster - gkn*, https://www.gknaerospace.com/se/produkter-och-tjaenster/, Accessed: 2026-01-23, 2026.

[2] G. Ortiz-de-Zárate et al., "Experimental and fem analysis of surface integrity when broaching ti64," *Procedia CIRP*, vol. 71, pp. 466–471, 2018, 4th CIRP Conference on Surface Integrity (CSI 2018). DOI: 10.1016/j.procir.2018.05.033. [Online]. Available: https://www.sciencedirect.com/science/article/pii/S2212827118304215.

[3] B. Denkena and D. Biermann, "Cutting edge geometries," *CIRP Annals*, vol. 63, no. 2, pp. 631–653, 2014, ISSN: 0007-8506. DOI: https://doi.org/10.1016/j.cirp.2014.05.009. [Online]. Available: https://www.sciencedirect.com/science/article/pii/S0007850614001917.

[4] P. Khanjanzadeh, H. Amirabadi, and J. Sadri, "Design of broaching tool using finite element method for achieving the lowest residual tensile stress in machining of ti6al4v alloy," *International Journal of Engineering*, vol. 33, no. 4, pp. 657–667, 2020, ISSN: 1025-2495. DOI: 10.5829/ije.2020.33.04a.17. [Online]. Available: https://www.ije.ir/article_106039.html.

[5] A. la Monaca, D. A. Axinte, Z. Liao, R. M'Saoubi, and M. C. Hardy, "Towards understanding the thermal history of microstructural surface deformation when cutting a next generation powder metallurgy nickel-base superalloy," *International Journal of Machine Tools and Manufacture*, vol. 168, p. 103 765, 2021, The Cutting of Metals: A Mechanics-Materials Viewpoint, ISSN: 0890-6955. DOI: https://doi.org/10.1016/j.ijmachtools.2021.103765. [Online]. Available: https://www.sciencedirect.com/science/article/pii/S0890695521000742.

[6] W. Grzesik, B. Kruszynski, and A. Ruszaj, "Surface integrity of machined surfaces," in Jan. 2010, pp. 143–179, ISBN: 978-1-84882-873-5. DOI: 10.1007/978-1-84882-874-2_5.

[7] National Transportation Safety Board, "Aircraft accident report: Uncontained engine failure, delta air lines flight 1288, mcdonnell douglas md-88, n927da, pensacola, florida, july 6, 1996," National Transportation Safety Board, Washington, D.C., Aircraft Accident Report NTSB/AAR-98/01, Jan. 1998, Notation 6725C, PB98-910401.

[8] C. A. Brice, "Unintended consequences: How qualification constrains innovation," National Aeronautics and Space Administration (NASA), Langley Research Center, Hampton, VA, Technical Memorandum NASA/TM-2026, 2011.

[9] Vinnova. "Digital platform för modellering av ytintegritet vid bearbetning av flygmotormaterial." Accessed: 2026-01-20, Sweden's Innovation Agency. [Online]. Available: https://www.vinnova.se/p/digital-platform-for-modellering-av-ytintegritet-vid-bearbetning-av-flygmotormaterial/.

[10] C.-F. Wyen, W. Knapp, and K. Wegener, "A new method for the characterisation of rounded cutting edges," *The International Journal of Advanced Manufacturing Technology*, vol. 59, no. 9–12, pp. 899–914, 2012. DOI: 10.1007/s00170-011-3555-4.

[11] X. Liang, Z. Liu, and B. Wang, "State-of-the-art of surface integrity induced by tool wear effects in machining process of titanium and nickel alloys: A review," *Measurement*, vol. 132, pp. 150–181, 2019, ISSN: 0263-2241. DOI: https://doi.org/10.1016/j.measurement.2018.09.045. [Online]. Available: https://www.sciencedirect.com/science/article/pii/S0263224118308807.

[12] H. K. Tönshoff and B. Denkena, *Basics of Cutting and Abrasive Processes*. Heidelberg: Springer-Verlag Berlin Heidelberg, 2013, ISBN: 978-3-642-33256-2. DOI: https://doi.org/10.1007/978-3-642-33257-9.

[13] C. Che-Haron and A. Jawaid, "The effect of machining on surface integrity of titanium alloy," *Journal of Materials Processing Technology*, vol. 166, no. 2, pp. 188–192, 2005, ISSN: 0924-0136. DOI: https://doi.org/10.1016/j.jmatprotec.2004.08.012. [Online]. Available: https://www.sciencedirect.com/science/article/pii/S0924013604010313.

[14] Z. Liao et al., "Surface integrity in metal machining - part i: Fundamentals of surface characteristics and formation mechanisms," *International Journal of Machine Tools and Manufacture*, vol. 162, p. 103 687, 2021, ISSN: 0890-6955. DOI: https://doi.org/10.1016/j.ijmachtools.2020.103687. [Online]. Available: https://www.sciencedirect.com/science/article/pii/S0890695520307021.

[15] Q. Shen, Z. Liu, Y. Hua, J. Zhao, W. Lv, and A. U. H. Mohsan, "Effects of cutting edge microgeometry on residual stress in orthogonal cutting of inconel 718 by fem," *Materials*, vol. 11, no. 6, 2018, ISSN: 1996-1944. DOI: 10.3390/ma11061015. [Online]. Available: https://www.mdpi.com/1996-1944/11/6/1015.

[16] CAM Tech, Inc., *Wire EDM for carbide components*, https://www.camtechedm.com/wire-edm-for-carbide-components/, Accessed: 2026-02-23, 2026.

[17] Xact Wire EDM Corporation, *What is wire EDM? | Electrical Discharge Machining*, https://www.xactedm.com/how-edm-works/, Accessed: 2026-02-24, 2026.

[18] *Basic quantities in cutting and grinding — part 1: Geometry of the active part of cutting tools — general terms, reference systems, tool and working angles, chip breakers*, Geneva, Switzerland: International Organization for Standardization, 1982. [Online]. Available: https://www.iso.org/standard/8052.html.

[19] M. Gerstenmeyer, B.-L. Ort, F. Zanger, and V. Schulze, "Influence of the cutting edge microgeometry on the surface integrity during mechanical surface modification by complementary machining," *Procedia CIRP*, vol. 58, pp. 55–60, 2017, 16th CIRP Conference on Modelling of Machining Operations, ISSN: 2212-8271. DOI: 10.1016/j.procir.2017.03.185.

[20] H. A. Kishawy, A. Hosseini, B. Moetakef-Imani, and V. P. Astakhov, "An energy based analysis of broaching operation: Cutting forces and resultant surface integrity," *CIRP Annals – Manufacturing Technology*, vol. 61, no. 1, pp. 107–110, 2012, ISSN: 0007-8506. DOI: 10.1016/j.cirp.2012.03.004.

[21] A. S. Ertürk, *Finite element metal cutting simulations*, PowerPoint presentation, PhD Student, Department of Industrial and Materials Science, Feb. 2026.

[22] D. J. Waldorf, R. E. DeVor, and S. G. Kapoor, "An evaluation of ploughing models for orthogonal machining," *Journal of Manufacturing Science and Engineering*, vol. 121, pp. 550–558, 1999.

[23] C. Fabián Pérez-Salinas, P. Fernández-Lucio, A. del Olmo, I. Aldekoa-Gallarza, and L. Norberto López de Lacalle, "The influence of cutting edge microgeometry on the broaching of inconel 718 slots," *Engineering Science and Technology, an International Journal*, vol. 48, p. 101 563, 2023, ISSN: 2215-0986. DOI: https://doi.org/10.1016/j.jestch.2023.101563. [Online]. Available: https://www.sciencedirect.com/science/article/pii/S2215098623002410.

[24] C. Hu, K. Zhuang, H. Elias-Birembaux, and J. Outeiro, "An improved numerical model for prediction of residual plastic strain in machining of ti6al4v titanium alloy concerning cutting edge microgeometries," *Procedia CIRP*, vol. 133, pp. 722–727, 2025, 20th CIRP Conference on Modeling of Machining Operations in Mons, ISSN: 2212-8271. DOI: https://doi.org/10.1016/j.procir.2025.02.123. [Online]. Available: https://www.sciencedirect.com/science/article/pii/S2212827125002124.

[25] Seco Tools, *Tool geometries make the machining difference*, https://www.secotools.com/article/tool_geometries_make_the_machining_difference, Accessed: 2026-01-21, n.d.

[26] Y. R. Shim et al., "Microstructure and mechanical properties of wire laser additive manufactured deposits and their tungsten inert gas welds," *Materials*, vol. 18, no. 6, 2025, Cited by: 1; All Open Access, Gold Open Access, Green Open Access. DOI: 10.3390/ma18061308. [Online]. Available: https://

www.scopus.com/inward/record.uri?eid=2-s2.0-105001138797&doi=10.3390%2fma18061308&partnerID=40&md5=60e61903266ea3a372f32e11383cc540.

[27] Bruker Austria GmbH, *Multiple edges in one measurement run - alicona*, Alicona_FOCUSvariation_magazine_2017_EN.pdf, Bruker Austria GmbH, Graz, Austria, 2026.

[28] V. Pednekar, V. Madhavan, and A. Adibi-Sedeh, "Investigation of the transition from plane strain to plane stress in orthogonal metal cutting," vol. 255, Jan. 2004. DOI: 10.1115/IMECE2004-62167.

[29] GROB-WERKE GmbH & Co. KG. "Universal machining center g350." Accessed: 2026-02-16. [Online]. Available: https://www.grobgroup.com/en/products/product-range/universal-machining-centers/milling-centers/g350/.

[30] N. Özbay, A. Ş. Yargıç, R. Z. Yarbay-Şahin, and E. Önal, "Full factorial experimental design analysis of reactive dye removal by carbon adsorption," *Journal of Chemistry*, vol. 2013, no. 1, p. 234 904, 2013. DOI: https://doi.org/10.1155/2013/234904. eprint: https://onlinelibrary.wiley.com/doi/pdf/10.1155/2013/234904. [Online]. Available: https://onlinelibrary.wiley.com/doi/abs/10.1155/2013/234904.

[31] Pennsylvania State University. "Stat 415 lesson 2.5: A t-interval for a mean," Accessed: 2026-05-15. [Online]. Available: https://online.stat.psu.edu/stat415/lesson/2/2.5.

[32] P. S. Prevéy and D. J. Hornbach, "X-ray diffraction residual-stress techniques," in *Materials Characterization*, ASM International, Dec. 2019, ISBN: 978-1-62708-213-6. DOI: 10.31399/asm.hb.v10.a0006632. eprint: https://dl.asminternational.org/handbooks/book/chapter-pdf/483247/a0006632.pdf. [Online]. Available: https://doi.org/10.31399/asm.hb.v10.a0006632.

[33] P. D. Berger, R. E. Maurer, and G. B. Celli, *Experimental Design: With Applications in Management, Engineering, and the Sciences*, 2nd ed. Cham, Switzerland: Springer International Publishing, 2018, ISBN: 978-3-319-64582-7. DOI: 10.1007/978-3-319-64583-4.

A

Appendix

Table A.1: Summary of contributing articles and research papers

Authors	Methodology	Topic/Conclusions
B. Denkena and D. Biermann [3]	Review and experiments	Definition of micro-geometry
B. Denkena and D. Biermann [3]	Review and experiments	Larger radius gives worse surface integrity
B. Denkena and D. Biermann [3]	Review and experiments	Larger radius gives larger compressive residual stress
Gertsenmeyer et al. [19]	Simulation experiments	κ<1 showed larger process forces
Kishawy et al. [20]	Broaching experiments	Larger process forces gives higher micro-hardness
A. S. Ertürk [21]	Simulations	• $\kappa < 1$ gives higher process forces • $\kappa > 1$ gives lower process forces • Higher S_α and S_γ gives higher process forces
Whyen et al. [10]	Theoretical model	Improved method for geometry characterization
A. S. Ertürk [21]	Simulations	Process forces reach steady state after 0.5 mm of engaged cut
D. J. Waldorf et al. [22]	Experimental study	A larger edge radius significantly raised the cutting force.

Authors	**Methodology**	**Topic/Conclusions**
Hu et al. [24]	Created a numerical prediction model	Larger radius generates deeper deformation

B

Appendix

Table B.1: Heat treatment recipe for test parts

Step	Temperature °C	Ramp time	Stationary time
1	600	1h 40 min	15 min
2	910	1h 15 min	15 min
3	940	15 min	58 min
4	390	25 min	30s
5	60	5 min	5 min

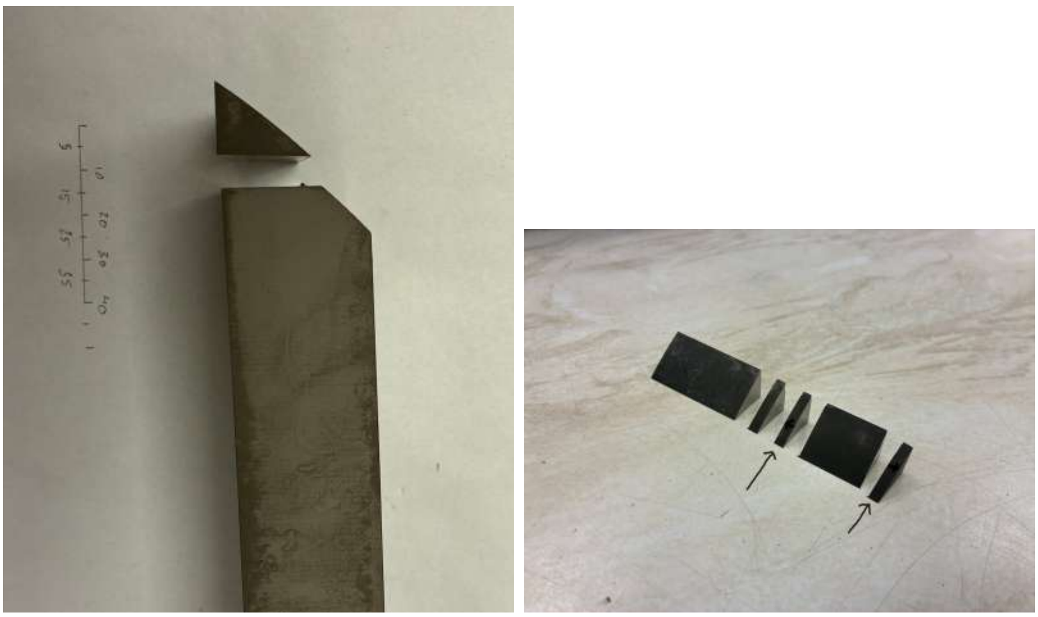

Figure B.1: Original position of the samples retrieved for looking at the phase structure of the material before experiments

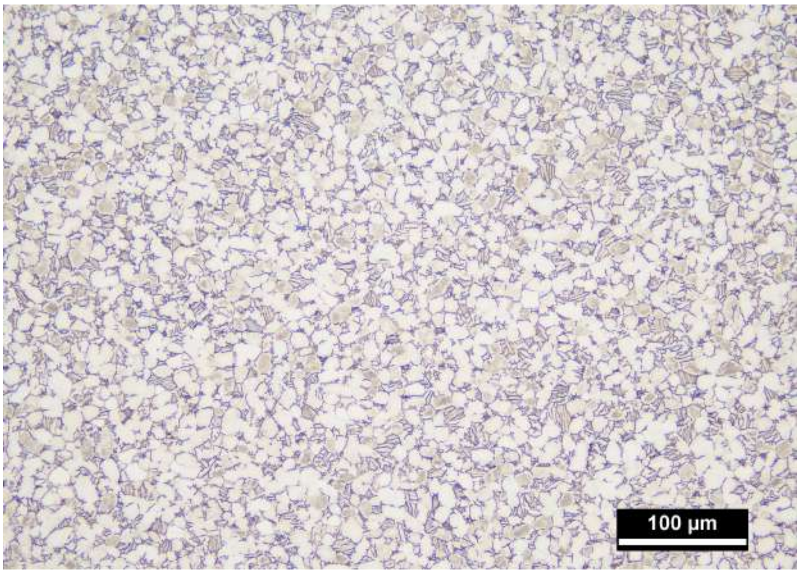

Figure B.2: Microstructure of material after heat treatment. Part closest to the edge.

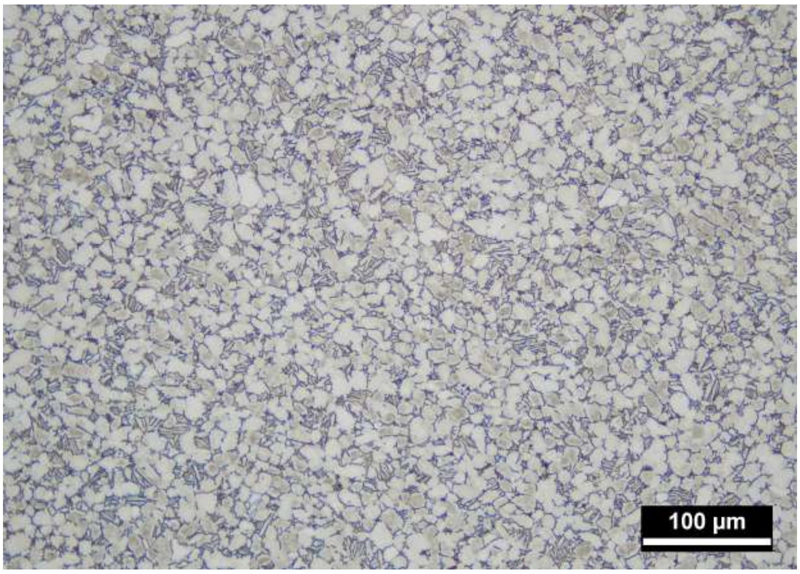

Figure B.3: Microstructure of material after heat treatment. Part retrieved from the middle.

Prior to machining, a hardness of the heat treated material was measured using the Vickers hardness method was performed. The average hardness was 319 HV0.3.

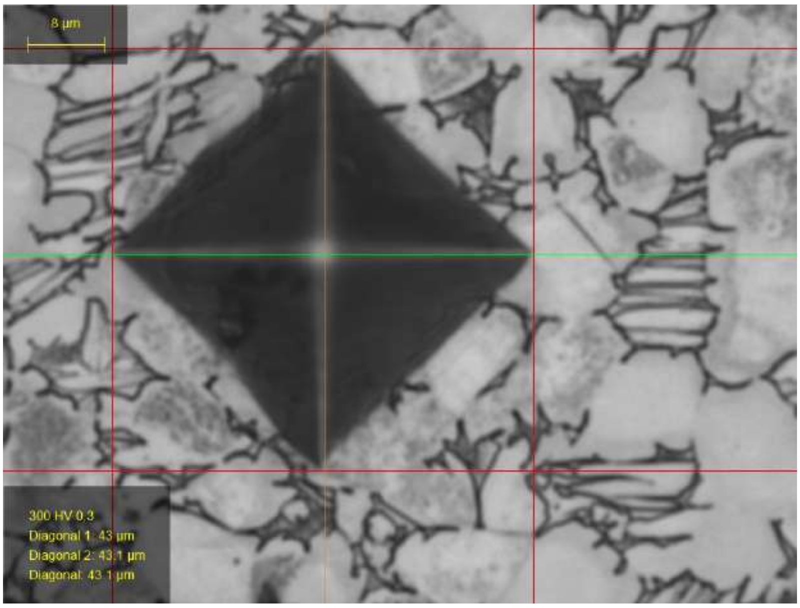

Figure B.4: Image taken on one out of five marks during the hardness testing.

C

Appendix

Table C.1: Updated DOE generated from MODDE. *Symmetry values are logarithmic with a base of 2.

Exp. No.	Radius	S*	Cutting Velocity	Cutting Depth
1	7.35	-0.0145	2.5	0.05
2	43.7	-1.737	2.5	0.05
3	8.5	1.31	2.5	0.05
4	44.4	1.74	2.5	0.05
5	7.35	-0.0145	10	0.05
6	43.7	-1.737	10	0.05
7	8.5	1.31	10	0.05
8	44.4	1.74	10	0.05
9	7.35	-0.0145	2.5	0.1
10	43.7	-1.737	2.5	0.1
11	8.5	1.31	2.5	0.1
12	44.4	1.74	2.5	0.1
13	7.35	-0.0145	10	0.1
14	43.7	-1.737	10	0.1
15	8.5	1.31	10	0.1
16	44.4	1.74	10	0.1
17	20	0.124	6.25	0.75
18	20	0.124	6.25	0.75
19	20	0.124	6.25	0.75

Table C.2: Mean total deformation depth, standard deviation, and 95% confidence interval for all experiments.

Exp. no.	Radius [µm]	S	a_f [mm]	v_c [m/min]	Mean [µm]	σ_{td} [µm]	95% CI
1	7.35	0.99	0.05	2.5	9.08	1.72	7.3–10.9
2	43.7	0.30	0.05	2.5	34.54	2.18	32.3–36.8
3	8.5	2.48	0.05	2.5	5.28	1.93	3.3–7.3
4	44.4	3.35	0.05	2.5	16.14	4.35	11.6–20.7
5	7.35	0.99	0.05	10.0	10.68	3.72	6.8–14.6
6	43.7	0.30	0.05	10.0	31.08	8.94	21.7–40.5
7	8.5	2.48	0.05	10.0	9.44	1.71	7.6–11.2
8	44.4	3.35	0.05	10.0	10.48	2.42	7.9–13.0
9	7.35	0.99	0.10	2.5	8.59	3.00	5.4–11.7
10	43.7	0.30	0.10	2.5	35.16	7.61	27.2–43.1
11	8.5	2.48	0.10	2.5	10.97	2.09	8.8–13.2
12	44.4	3.35	0.10	2.5	15.24	3.54	11.5–19.0
13	7.35	0.99	0.10	10.0	5.54	1.03	4.5–6.6
14	43.7	0.30	0.10	10.0	37.08	6.13	30.6–43.5
15	8.5	2.48	0.10	10.0	6.39	1.01	5.3–7.5
16	44.4	3.35	0.10	10.0	12.32	1.43	10.8–13.8
17	20.0	1.09	0.075	6.25	13.86	2.92	10.8–16.9
18	20.0	1.09	0.075	6.25	13.48	1.34	12.1–14.9
19	20.0	1.09	0.075	6.25	13.58	2.50	11.0–16.2

Table C.3: Mean total deformation depth, standard deviation, and 95% confidence interval for all experiments.

Exp. no.	Radius [µm]	S	a_f [mm]	v_c [m/min]	Mean [µm]	σ_{td} [µm]	95% CI
1	7.35	0.99	0.05	2.5	9.08	1.72	7.3–10.9
2	43.7	0.30	0.05	2.5	34.54	2.18	32.3–36.8
3	8.5	2.48	0.05	2.5	5.28	1.93	3.3–7.3
4	44.4	3.35	0.05	2.5	16.14	4.35	11.6–20.7
5	7.35	0.99	0.05	10.0	10.68	3.72	6.8–14.6
6	43.7	0.30	0.05	10.0	31.08	8.94	21.7–40.5
7	8.5	2.48	0.05	10.0	9.44	1.71	7.6–11.2
8	44.4	3.35	0.05	10.0	10.48	2.42	7.9–13.0
9	7.35	0.99	0.10	2.5	8.59	3.00	5.4–11.7
10	43.7	0.30	0.10	2.5	35.16	7.61	27.2–43.1
11	8.5	2.48	0.10	2.5	10.97	2.09	8.8–13.2
12	44.4	3.35	0.10	2.5	15.24	3.54	11.5–19.0
13	7.35	0.99	0.10	10.0	5.54	1.03	4.5–6.6
14	43.7	0.30	0.10	10.0	37.08	6.13	30.6–43.5
15	8.5	2.48	0.10	10.0	6.39	1.01	5.3–7.5
16	44.4	3.35	0.10	10.0	12.32	1.43	10.8–13.8
17	20.0	1.09	0.075	6.25	13.86	2.92	10.8–16.9
18	20.0	1.09	0.075	6.25	13.48	1.34	12.1–14.9
19	20.0	1.09	0.075	6.25	13.58	2.50	11.0–16.2

Table C.4: Mean measured amorphous layer, standard deviation, and 95% confidence interval from experiments with no lubrication.

Exp. no.	Radius [µm]	S	a_f [mm]	v_c [m/min]	Mean [µm]	σ_{sd} [µm]	95% CI
20	20.0	1.09	0.075	6.25	3.04	0.98	2.0–4.1
26	43.7	0.30	0.05	2.5	11.23	3.45	7.6–14.9
27	8.5	2.48	0.05	2.5	0.00	0.00	0.0–0.0
28	43.7	0.30	0.10	2.5	12.93	1.00	11.9–14.0
29	8.5	2.48	0.10	2.5	0.00	0.00	0.0–0.0

Table C.5: Mean total deformation depth, standard deviation, and 95% confidence interval for experiments with no lubrication.

Exp. no.	Radius [µm]	S	a_f [mm]	v_c [m/min]	Mean [µm]	σ_{td} [µm]	95% CI
20	20.0	1.09	0.075	6.25	12.45	2.01	10.3–14.6
26	43.7	0.30	0.05	2.5	40.06	6.74	33.0–47.1
27	8.5	2.48	0.05	2.5	8.01	1.31	6.6–9.4
28	43.7	0.30	0.10	2.5	43.97	9.28	34.2–53.7
29	8.5	2.48	0.10	2.5	10.18	1.58	8.5–11.8

Table C.6: Mean measured amorphous layer, standard deviation, and 95% confidence interval from experiments with zero depth-of-cut.

Exp. no.	Radius [µm]	S	a_f [mm]	v_c [m/min]	Mean [µm]	σ_a [µm]	95% CI
21	20.0	1.09	0.00	2.5	2.00	1.21	0.7–3.3
22	7.35	0.99	0.00	2.5	0.51	0.79	0.0–1.3
23	43.7	0.30	0.00	2.5	0.74	1.15	0.0–2.0
24	8.5	2.48	0.00	2.5	0.00	0.00	0.0–0.0
25	44.4	3.35	0.00	2.5	3.11	1.65	1.4–4.8

Table C.7: Mean total deformation, standard deviation, and 95% confidence interval for experiments with zero-depth-of-cut.

Exp. no.	Radius [µm]	S	a_f [mm]	v_c [m/min]	Mean [µm]	σ_{td} [µm]	95% CI
21	20.0	1.09	0.00	2.5	10.45	1.81	8.5–12.4
22	7.35	0.99	0.00	2.5	13.18	3.48	9.5–16.8
23	43.7	0.30	0.00	2.5	10.84	1.79	9.0–12.7
24	8.5	2.48	0.00	2.5	7.41	1.28	6.1–8.8
25	44.4	3.35	0.00	2.5	15.23	2.23	12.9–17.6

Table C.8: Mean, standard deviation, and 95% confidence interval for number of measured surface tears in experiments 1–19.

Exp. no.	Radius [µm]	S	a_f [mm]	v_c [m/min]	Mean	σ_{st}	95% CI
1	7.35	0.99	0.05	2.5	13.0	8.7	3.9–22.1
2	43.7	0.30	0.05	2.5	4.8	6.4	0.0–11.5
3	8.5	2.48	0.05	2.5	8.0	4.3	3.5–12.5
4	44.4	3.35	0.05	2.5	7.2	3.0	4.1–10.3
5	7.35	0.99	0.05	10.0	3.4	2.3	1.0–5.8
6	43.7	0.30	0.05	10.0	5.3	5.0	0.1–10.5
7	8.5	2.48	0.05	10.0	2.5	1.4	1.0–4.0
8	44.4	3.35	0.05	10.0	7.5	5.7	1.5–13.5
9	7.35	0.99	0.10	2.5	18.0	14.2	3.1–32.9
10	43.7	0.30	0.10	2.5	9.7	4.0	5.5–13.9
11	8.5	2.48	0.10	2.5	11.2	5.9	5.0–17.4
12	44.4	3.35	0.10	2.5	8.0	3.2	4.6–11.4
13	7.35	0.99	0.10	10.0	3.3	3.1	0.0–6.6
14	43.7	0.30	0.10	10.0	5.2	3.1	1.9–8.5
15	8.5	2.48	0.10	10.0	8.5	3.1	5.2–11.8
16	44.4	3.35	0.10	10.0	11.7	7.6	3.7–19.7
17	20.0	1.09	0.075	6.25	4.2	3.9	0.1–8.3
18	20.0	1.09	0.075	6.25	5.0	0.0	5.0–5.0
19	20.0	1.09	0.075	6.25	2.0	1.8	0.1–3.9

Table C.9: Mean, standard deviation, and 95% confidence interval for number of measured re-deposited material features in experiments 1–19.

Exp. no.	Radius [µm]	S	a_f [mm]	v_c [m/min]	Mean	σ	95% CI
1	7.35	0.99	0.05	2.5	31.8	15.5	15.5–48.1
2	43.7	0.30	0.05	2.5	12.7	9.1	3.1–22.3
3	8.5	2.48	0.05	2.5	16.3	8.4	7.5–25.1
4	44.4	3.35	0.05	2.5	19.0	6.4	12.3–25.7
5	7.35	0.99	0.05	10.0	12.0	18.4	0.0–31.3
6	43.7	0.30	0.05	10.0	13.8	10.6	2.7–24.9
7	8.5	2.48	0.05	10.0	5.5	2.4	3.0–8.0
8	44.4	3.35	0.05	10.0	10.5	4.8	5.5–15.5
9	7.35	0.99	0.10	2.5	40.5	10.3	29.7–51.3
10	43.7	0.30	0.10	2.5	13.7	6.1	7.3–20.1
11	8.5	2.48	0.10	2.5	22.3	12.1	9.6–35.0
12	44.4	3.35	0.10	2.5	9.5	3.8	5.5–13.5
13	7.35	0.99	0.10	10.0	11.7	7.1	4.2–19.2
14	43.7	0.30	0.10	10.0	10.0	5.1	4.6–15.4
15	8.5	2.48	0.10	10.0	23.8	11.6	11.6–36.0
16	44.4	3.35	0.10	10.0	24.3	20.4	2.9–45.7
17	20.0	1.09	0.075	6.25	14.8	9.3	5.0–24.6
18	20.0	1.09	0.075	6.25	17.0	0.0	17.0–17.0
19	20.0	1.09	0.075	6.25	7.5	6.7	0.5–14.5

Table C.10: Mean, standard deviation, and 95% confidence interval for number of measured surface tearing features in experiments with no lubrication.

Exp. no.	Radius [µm]	S	a_f [mm]	v_c [m/min]	Mean	σ_{st}	95% CI
20	20.0	1.09	0.075	6.25	3.5	2.9	0.5–6.5
26	43.7	0.30	0.05	2.5	5.0	5.5	0.0–10.8
27	8.5	2.48	0.05	2.5	18.2	5.3	12.6–23.8
28	43.7	0.30	0.10	2.5	2.8	4.1	0.0–7.1
29	8.5	2.48	0.10	2.5	21.4	6.4	14.7–28.1

Table C.11: Mean, standard deviation, and 95% confidence interval for number of measured re-deposited features in experiments with no lubrication.

Exp. no.	Radius [µm]	S	a_f [mm]	v_c [m/min]	Mean	σ_{rd}	95% CI
20	20.0	1.09	0.075	6.25	8.5	3.6	4.7–12.3
26	43.7	0.30	0.05	2.5	12.0	13.7	0.0–26.4
27	8.5	2.48	0.05	2.5	19.5	11.4	7.5–31.5
28	43.7	0.30	0.10	2.5	4.0	1.9	2.0–6.0
29	8.5	2.48	0.10	2.5	12.2	5.0	7.0–17.4

Table C.12: Mean, standard deviation, and 95% confidence interval for number of measured surface tear features in experiments with zero depth-of-cut.

Exp. no.	Radius [µm]	S	a_f [mm]	v_c [m/min]	Mean	σ_{st}	95% CI
21	20.0	1.09	0.00	2.5	8.0	7.0	0.7–15.3
22	7.35	0.99	0.00	2.5	10.7	4.7	5.8–15.6
23	43.7	0.30	0.00	2.5	13.0	5.4	7.3–18.7
24	8.5	2.48	0.00	2.5	24.8	9.5	14.8–34.8
25	44.4	3.35	0.00	2.5	9.7	3.7	5.8–13.6

Table C.13: Mean, standard deviation, and 95% confidence interval for number of measured re-deposited features in experiments with zero depth-of-cut.

Exp. no.	Radius [µm]	S	a_f [mm]	v_c [m/min]	Mean	σ_{rd}	95% CI
21	20.0	1.09	0.00	2.5	9.3	6.1	2.9–15.7
22	7.35	0.99	0.00	2.5	16.7	9.2	7.0–26.4
23	43.7	0.30	0.00	2.5	19.0	15.2	3.0–35.0
24	8.5	2.48	0.00	2.5	12.8	5.3	7.2–18.4
25	44.4	3.35	0.00	2.5	14.2	13.5	0.0–28.4

Table C.14: Model validation metrics for the fitted regression models. Data from MODDE.

Response variable	N	DF	R^2	R^2_{adj}	Q^2	RSD	Cond. No.
Total deformation	19	15	0.962	0.955	0.935	2.223	4.577
Amorphous layer	19	10	0.906	0.831	0.761	1.195	4.577
Surface tearing	19	12	0.664	0.495	0.300	2.908	2.173
Re-deposited material	19	15	0.417	0.300	0.045	7.297	1.518
F_x	19	11	0.925	0.876	0.774	67.14	4.577
F_z	19	11	0.988	0.980	0.974	76.13	4.577
Long. σ_{res}	19	13	0.715	0.605	0.332	212.9	4.177
Cross. σ_{res}	19	13	0.679	0.555	0.345	209.6	4.177

DEPARTMENT OF MECHANICAL ENGINEERING
CHALMERS UNIVERSITY OF TECHNOLOGY
Gothenburg, Sweden
www.chalmers.se

CHALMERS
UNIVERSITY OF TECHNOLOGY